Research papers

Mechanically and accurately calculate river width in vegetation areas by coupling Sentinel-1 and -2 imageries within land-water-mixed pixels

Maomao Li [a], Changsen Zhao [a,d,e,*], Zhen Duan [f], Hongguang Cheng [a], Yanqing Lian [b], Guoqing Wang [c]

[a] College of Water Sciences, Beijing Normal University, Beijing 100875, PR China
[b] Yangtze Institute for Conservation and Development, Hohai University, Nanjing 210098, Jiangsu, PR China
[c] The National Key Laboratory of Water Disaster Prevention, Nanjing Hydraulic Research Institute, Nanjing 210098, Jiangsu, PR China
[d] ICube, UdS, CNRS (UMR 7357), 300 Bld Sebastien Brant, CS 10413, 67412 Illkirch, France
[e] School of Environment & Sustainability, University of Saskatchewan, Saskatoon SK S7N 5C9, Canada
[f] Tai'an Hydrological Center, Tai'an 271000, PR China

ARTICLE INFO

ABSTRACT

Accurately measuring river width has been one of greatest challenges due to the presence of mixed land–water pixels intersecting river boundaries. Therefore, this study proposed a novel mechanical method (RW-vebasud), instead of traditionally empirical models, to estimate river width within a pixel in vegetation areas based on time series analysis of Sentinel-1 and Sentinel-2 spaceborne multispectral images. We initially explored the mechanism of variation in backscatter intensity (σ) with enhanced vegetation index (EVI) whereby we successfully removed noises in σ–EVI relationship resulted from vegetation growth. Then, for the first time a smooth functional relationship between water area proportion and backscatter intensity within a ROI (or region of interest) was constructed. Consequently, subpixel water–land separation based on the mechanism process was realized. The novel method could not only work at large-scaled rivers (satellite-visible) but perform well at small-scaled rivers within a water-land mixed pixel (satellite-invisible). A total of 197 measurements for river widths in China during 2016 ~ 2021 were used for model verification, demonstrating a positive correlation between EVI and σ, with R^2 ranging from 0.16 to 0.69 (P<0.05). The RW-vebasud exhibited superior accuracy in calculating river width compared to the widely used MNDWI (modified normalized difference water index). The Root Mean Square Error (RMSE) decreased by 4.32 ~ 6.65 m when the river width was less than 90 m and by 66.12 % when it exceeded 90 m, compared to MNDWI. Remarkably, RW-vebasud maintains satisfactorily high accuracy (the Nash-Sutcliffe efficiency coefficient: NSE=0.70 and RMSE=3.19) even at the spatial scale less than 3 times the image resolution, breaking the internationally accepted limit that river width extraction can only be accurate when the river width is greater than 3 times the satellite resolution. Moreover, the accuracy of this method is better than that with the currently well-known global river width datasets GRWL and MERIT Hydro. For the RW-Vebasud/GRWL/MERIT Hydro datasets, the NSE=0.99 /0.93/0.87, the RMSE=5.99/42.33/54.27, and the R^2 = 0.99/0.91/0.74, respectively. The application of RW-vebasud in China shows that river widths in wet and dry seasons exhibited an increasing trend over the previous six years (2016–2021), as global warming accelerated glacier melting and increased rainfall quantity, with an average growth rate of 2.26 m/year (wet, P<0.05) and 2.17 m/year (dry, P<0.05), respectively. In response to the summer/winter Asian monsoons, most rivers widen in summer. The largest river width occurs in the Yellow River Basin (YLRB, 155.28 m on average), while the smallest occurs in the Hai River Basin (HARB, 22.99 m on average). The method proposed in this study can provide efficient techniques for surface river-width reconstruction which can greatly facilitate global resource and environmental modelling.

* Corresponding author.
    E-mail address: hzjohnson2003@163.com (C. Zhao).

1. Introduction

Global resource and environmental modelling in terms of biogeo-chemical cycle and carbon emission reduction are essential for sustainable development of society and economy. Rivers serving as primary pathways for water and nutrient transportation from land to the ocean, play significant roles in biogeochemical cycle and water-atmosphere carbon movement (Ling et al., 2019; Yang et al., 2020; Messager et al., 2021). River width, as one of the most important river parameters essential for water-related hazards prevention (Huang et al., 2018; Verma et al., 2021; Durand et al., 2023), affects the rates of biogeo-chemical exchange and carbon dioxide movement (Allen et al., 2018; Raymond et al., 2013).

River width data acquisition methods are mainly divided into two categories: field measurement methods and remote sensing image extraction methods. Field measurement methods are often laborious, time-consuming, costly and face challenges related to rugged terrain (Yang et al., 2020; Tarpanelli et al., 2023), thus limiting their wide application. Extracting river width data based on remote sensing images provides a cost-effective alternative (Stumpf et al., 2016; Ling et al., 2019; Verma et al., 2021). The precision of river width measurement through remote sensing primarily depends on the strength of the algorithm employed to recognize river (Yang et al., 2020). The algorithm can be classified as threshold method, classifier method and automatic method. The threshold method is used to classify remote sensing images from the spectral information of images. At present, water index methods (MNDWI and AWEI) and OTSU methods are commonly used (Wang et al., 2021). The main classifier methods are the support vector machine (SVM) and decision tree (CART) (Yu et al., 2022). The automatic method combines the threshold method and the classifier method, using a global–local idea to automatically extract information from large areas and large-scale water areas (Lu et al., 2021; Pavelsky and Smith, 2008). In recent studies, the feasibility of using these methods to estimate river width by remote sensing has been successfully demonstrated. Scholars have used single-sensor satellite data of different resolutions, e. g., 250 m moderate resolution imaging spectroradiometer (MODIS) data (Pavelsky and Smith, 2008), synthetic aperture radar (SAR) images (Verma et al., 2021), and 30 m Landsat imagery (Allen and Pavelsky, 2018; Hou et al., 2019), to produce a series of river width datasets, including the MERIT Hydro datasets (Yamazaki et al., 2019), the North American River Width (NARWidth) dataset (Allen and Pavelsky, 2015), and the Global River Widths from Landsat (GRWL) Database (Allen and Pavelsky, 2018), etc. However, single-sensor satellites have limitations in comprehensive parameter retrieval, and are difficult to handle complex environments. Combining SAR and optical data allows for leveraging the strengths of both sensors, reducing errors from single data sources, and enhancing the accuracy and reliability of river width calculations (Tarpanelli et al., 2022; Orusa et al., 2023).

Despite the widespread use of these methods, large errors often occur because these methods depend heavily on the resolution of the image itself. Due to the limited spatial resolution of available noncommercial satellite imagery, accurately measuring the width of narrow rivers (width < 30 m) remains a challenging task (Lin et al., 2020; Lu et al., 2021; Sun et al., 2018). During the space-based measurement of river width, errors are commonly introduced in the pixels where water and land appear intermixed. The reason is that a river boundary often runs through image pixels instead of following their edges; consequently, a river boundary is difficult to capture well (Foody et al., 2005; Ling et al., 2019; Yin et al., 2022). Consequently, remote sensing imagery faces challenges in accurately identifying hydraulically invisible small rivers, particularly those that have widths narrower than the resolution of a single pixel (e.g., <10 m for Sentinel, a noncommercial satellite). They can only be identified by field measurements, drone flights or high-resolution commercial satellites. Acquiring such high-resolution images is often constrained by factors such as limited financial resources, time constraints, governmental policies, and geographical limitations.

These obstacles hinder the widespread adoption and practical application of high-resolution remote sensing imagery. These factors have resulted in significant underestimations the importance of river networks in biogeochemical cycles (Zhao et al., 2019; Wang et al., 2021; Lu et al., 2021). Therefore, to overcome the challenge of accurately measuring river width in cases where the rivers are narrower than the spatial resolution of the remotely sensed imagery, scientists began to use the subpixel decomposition method to improve the precision of river width extraction (Ling et al., 2019). The current mainstream methods for spectral unmixing include Linear Spectral Mixture Model and Nonlinear Spectral Mixture Mode. However, these methods heavily rely on accurate spectral information and mixing pixel proportions, often leading to unclear physical interpretations. These issues severely hinder research on water resource management, water hazard prevention and carbon dioxide movement across the world, especially in data-scarce hydraulically invisible small river areas of China. Therefore, there is an urgent need to develop a new mechanistic subpixel decomposition method that is less dependent on ground observation data and can be widely applied.

From a mechanistic perspective, for vegetation regions containing water bodies, their spectral characteristics primarily depend on water and vegetation. The spectral properties of unit area water bodies show minimal temporal variation (Canisius et al., 2018; DeVries et al., 2020), whereas vegetation spectral characteristics are highly sensitive to vegetation structural features (Van Tricht et al., 2018; Zhou et al., 2019). Spectral properties vary temporally and spatially with vegetation growth and distribution. Vegetation grows throughout the year, differing in spatial vegetation types and canopy structures, leading to uncertainty in the relationship between vegetation feature parameters and spectral properties. Hence, vegetation spectral characteristics are temporally and spatially unstable, posing challenges and uncertainties in spectral unmixing (Harfenmeister et al., 2019; Nguyen et al., 2016; Tao et al., 2016). Thus, this study aims to propose a globally-applicable method for decomposing vegetated land–water mixed pixels, independent of ground observations and with physical mechanisms to enhance river width inversion precision by eliminating the impact of vegetation growth. In this paper, (1) the key factors that affect the change in river width are analyzed, the influence mechanism and model are determined, a calculation framework is built, and the river width is calculated; (2) the accuracy of the method is calculated, and the uncertainty of the method is analyzed based on measuring river widths; (3) the river width of nine typical river basins (including hydraulically invisible small rivers) in China from 2016 to 2021 are calculated using the verified method, and the spatiotemporal variation characteristics are analyzed. The outcome of this study could greatly facilitate policy-making in terms of water-related hazards prevention, biogeochemical cycle and carbon emission reduction across the world.

2. Study area

China, with a land area of over 9.6 million km^2, features low-lying topography from west to east (Wang and LinHo, 2002; Yang et al., 2020). China has approximately 50,000 rivers, including a multitude of exterior rivers, and is geographically stratified into nine basins: the Songliao River Basin (SLRB), Hai River Basin (HARB), Inland River Basin (INRB), Yellow River Basin (YLRB), Huai River Basin (HURB), South–West River Basin (SWRB), Yangtze River Basin (YZRB), South–East River Basin (SERB) and Pearl River Basin (PERB) (Yang et al., 2020). Since river width extraction is more accurate at more than 3 times the satellite resolution (Allen and Pavelsky, 2018), we classified all rivers by river width based on 10 m resolution Sentinel data as follows: large river (LR) (>90 m), middle river (MR) (30 ~ 90 m), small river (SR) (10 ~ 30 m), and narrow river (NR) (<10 m). To facilitate the analysis of river width differences among river basins in China, we randomly and evenly selected 197 representative sections on grade 1–5 rivers. The river and representative section distributions are shown in Fig. 1.
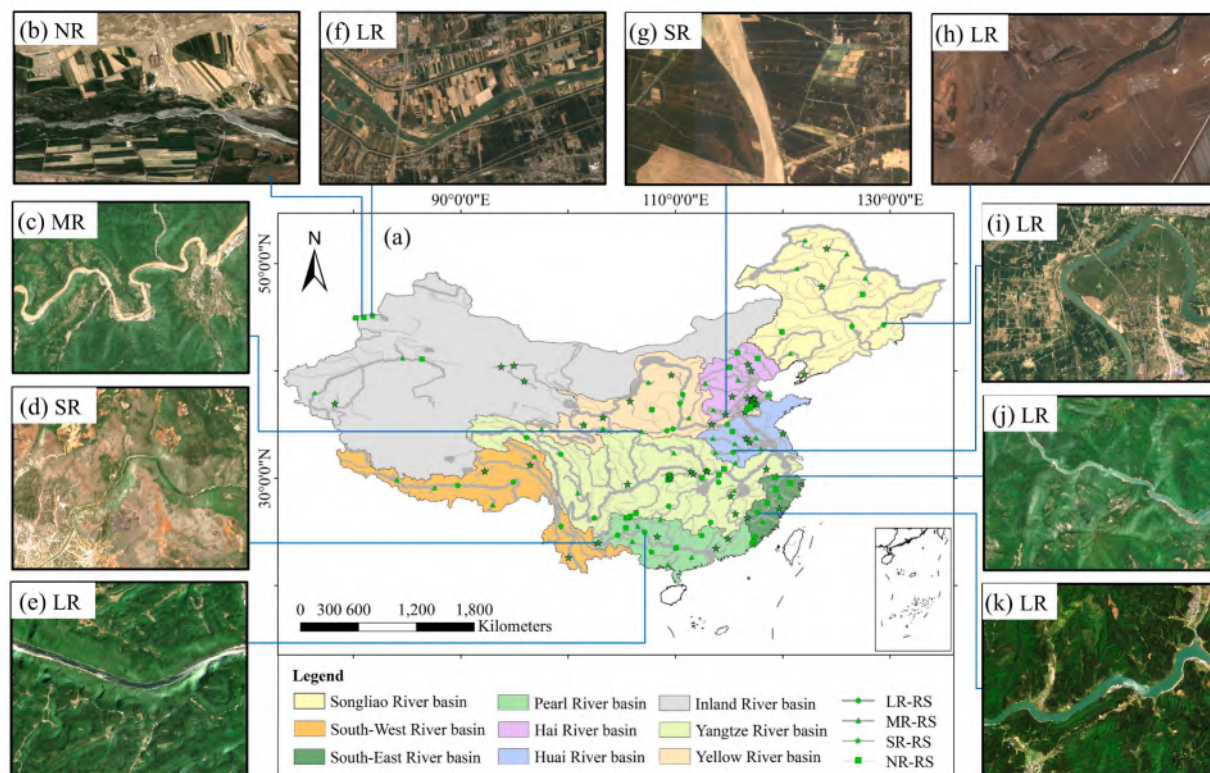
Fig. 1. Representative sections on grade 1–5 rivers from nine basins in China. (a) shows the location of sites and (b)-(k) are true color images from Sentinel-2. LR-RS: large river and representative section, MR-RS: middle river and representative section, SR-RS: small river and representative section, and NR-RS: narrow river and representative section.

3. Materials and methods

3.1. Data

3.1.1. Sentinel-1 and -2 data

Among noncommercial satellites, compared with Landsat and MODIS, the Sentinel satellite system, an open access data source, can obtain both radar and optical images with relatively fine spatial resolution (~10 m) and high update frequency, or temporal resolution, (~5d) (Wang et al., 2019; Yesou et al., 2016). Recently, Sentinel-1 and -2 image data have been widely used in flood monitoring, crop growth monitoring and so on (DeVries et al., 2020; Song et al., 2021). Therefore, Sentinel-1 and -2 images were used for subpixel decomposition in this paper to greatly enhance the precision and effectiveness of river width extraction.

We obtained 6090 scenes of images from Sentinel-1 and -2 during the timeframe spanning from January 2016 to December 2021. The data were retrieved from the Google Earth Engine (GEE) web platform (Gorelick et al., 2017). The radiometric terrain correction (RTC) is done in GEE to mitigate the influence of terrain on backscatter (Small, 2011; Vollrath et al., 2020). In this paper, the Sentinel-1 backscatter intensity parameter was used, with a range of (0, $+\infty$) (DeVries et al., 2020).

We utilized the top-of-atmosphere datasets from January 2016 to November 2018 and the surface reflectance dataset from December 2018 to December 2021 of Sentinel-2, provided by the European Space Agency (ESA). The top-of-atmosphere datasets was atmospherically corrected using the Second Simulation of Satellite Signal in the Solar Spectrum (6S) model prior to its use (Vermote et al., 1997). Spectral bands 2 (blue), 3 (green), 4 (red), 8 (near infrared), and 11 (shortwave infrared) were employed to compute the enhanced vegetation index (EVI), modified normalized difference water index (MNDWI), and fraction of vegetation cover (FVC). Among them, band 11 (with a

resolution of 20 m) was resampled to 10 m before conducting calculations. In the optical bands (bands 2, 3 and 4) large cloud proportion in an image always lowers the accuracy of calculated river width (Lu et al., 2022). Thus, we adopted the ratio of cloudy to total pixel number in a buffer of 5 km at each river section (Huang et al., 2018), to help select images. Based on the Fmask algorithm, only images covering the section buffer with an index less than 20 % were selected.

3.1.2. Measured data

In this study, the river width data measured via OvitalMap and in situ stations were used as standards to verify the river width calculated by our proposed method. OvitalMap is a map browsing application compatible with multiple platforms, utilizing the Google API as its foundation (Liu et al., 2021). We used 19-level data (resolution 0.30 m) to measure the values of river width in space from Jan. 2018 to Dec. 2019. As shown in Fig. 1, a total of 197 sets of water surface width data were obtained. We also obtained measurements from 6 sites in Jinan from May to November 2016 and 11 sets of water width data, and the range of water surface width variation for all sites was 1.46 ~ 569.76 m. For details, see Table 1 and Fig. 1.

*LR: large river (river width > 90 m); MR: middle river (30 m < river width < 90 m); SR: small river (10 m < river width < 30 m); and NR: narrow river (river width < 10 m).

3.2. Method

This paper proposed a new framework named river width with vegetation-backscattered-coefficient-based subpixel decomposition (RW-vebasud) to decompose mixed river and vegetated land pixels to improve the precision of river width estimation by satellites. The detailed process of the method is illustrated in Fig. 2. First, large rivers (river width > 90 m) were selected, the region of interest (ROI) of each

Table 1
Satellite data and ground measurement data.

Data	Source	River width classification	Site number	Spatial resolution	Period
Sentinel-1	GEE	/	/	10 m	01/
Sentinel-2	GEE	/	/	10 m	2016–12/ 2021
Measured river width	Ovitalmap	LR	45	0.30 m	01/ 2018–12/ 2019
		MR	40		
		SR	55		
		NR	57		
	In situ	NR	11	/	05/ 2016–11/ 2016

*LR: large river (river width > 90 m); MR: middle river (30 m < river width < 90 m); SR: small river (10 m < river width < 30 m); and NR: narrow river (river width < 10 m).

river was determined according to the vegetation distribution. Moreover, the relationship between the EVI and the backscatter intensity (σ) of the nonaqueous area of the ROI was established based on the mechanism of the variation of σ with the vegetation index, whereby the interference of vegetation growth on σ was eliminated, and the stable backscatter intensity series of the nonaqueous region, which is not affected by vegetation growth, was obtained. The backscatter intensity of the overall ROI varying only with the ratio of the water body ($\sigma_{ROI, noveg}$) and not disturbed by vegetation growth, was then calculated to establish the functional relationship between the water body percentage (A_W/A_{ROI}, where A_W is the water body area within the ROI and A_{ROI} is the area of the ROI) and $\sigma_{ROI,noveg}$ ($A_W/A_{ROI}\sim\sigma_{ROI,noveg}$). And the relationship between the ratio of mean FVC values inside the ROI to those of neighboring pixels and $\sigma_{ROI,noveg}$ was established to calculate $\sigma_{ROI,noveg}$. Finally, by combining the two functional relationships derived from

large rivers mentioned above and applying them to mixed pixel scales, it is possible to accurately calculate the water proportion of any river section within the study area. The water surface width was obtained based on the water body percentage (A_w/A_{ROI}) of any river sections in the study area.

3.2.1. Selection of the region of interest

To calculate the river width accurately, we selected a relatively straight river section with vegetation distribution on both sides. A single row of pixels, larger than the temporally maximum river width and perpendicular to the direction of river flow, was selected as the region of interest (ROI) to ensure that the selected row was covered by vegetation on both sides of the river. This can minimize the impact of soil moisture variation on the σ, to ensure that the backscattering within ROI changes only with the percentage of water and vegetation area. Additionally, since the selected areas in this study are all flat and covered in vegetation, with nearly identical topographic relief and soil roughness within each ROI, the influence of these factors on σ was neglected. And we visually identified the multi-year (2016–2021) maximum water extent (corresponding to the maximum river width) based on MNDWI water surface data using Sentinel-2 images (taking partial river sections and time as examples in Fig. 3).

3.2.2. Mechanism analysis of the variation in backscatter intensity (σ) with the EVI and establishment of the correlation

The total backscatter intensity of each ROI with vegetation cover exhibits variations depending on the ratio of vegetation to water area. As the backscatter intensity per unit area of water is basically constant, the water area backscatter intensity only varies with the water area, i.e., with time. Therefore, as long as backscatter intensity of vegetation area in a ROI is obtained, the water area backscatter intensity can be calculated and then the river width in the ROI can be obtained based on the
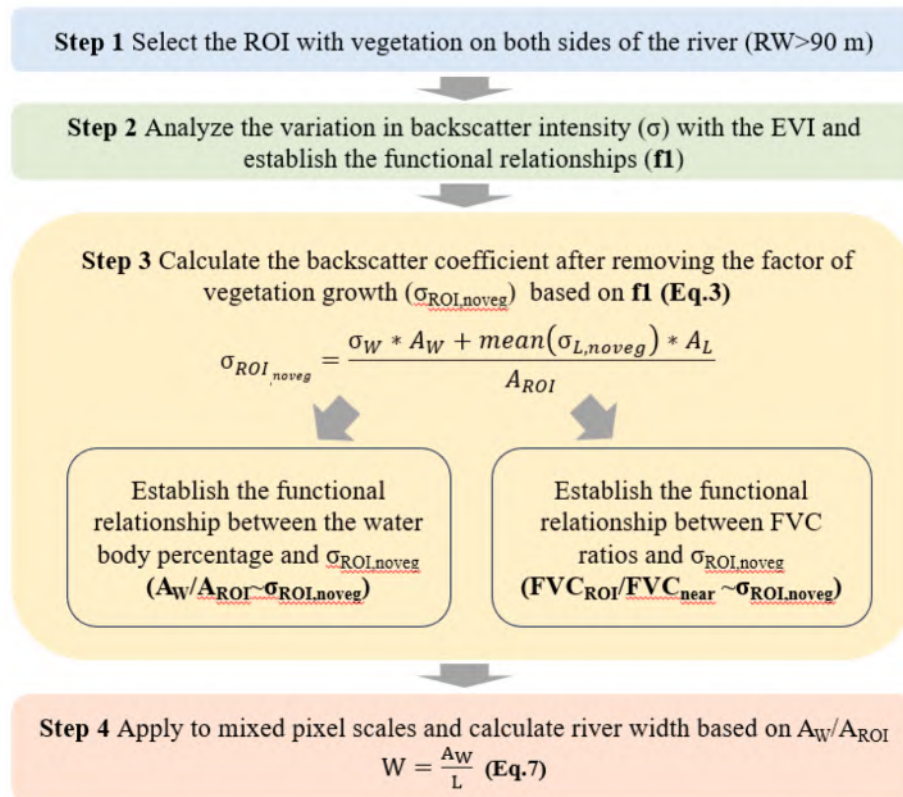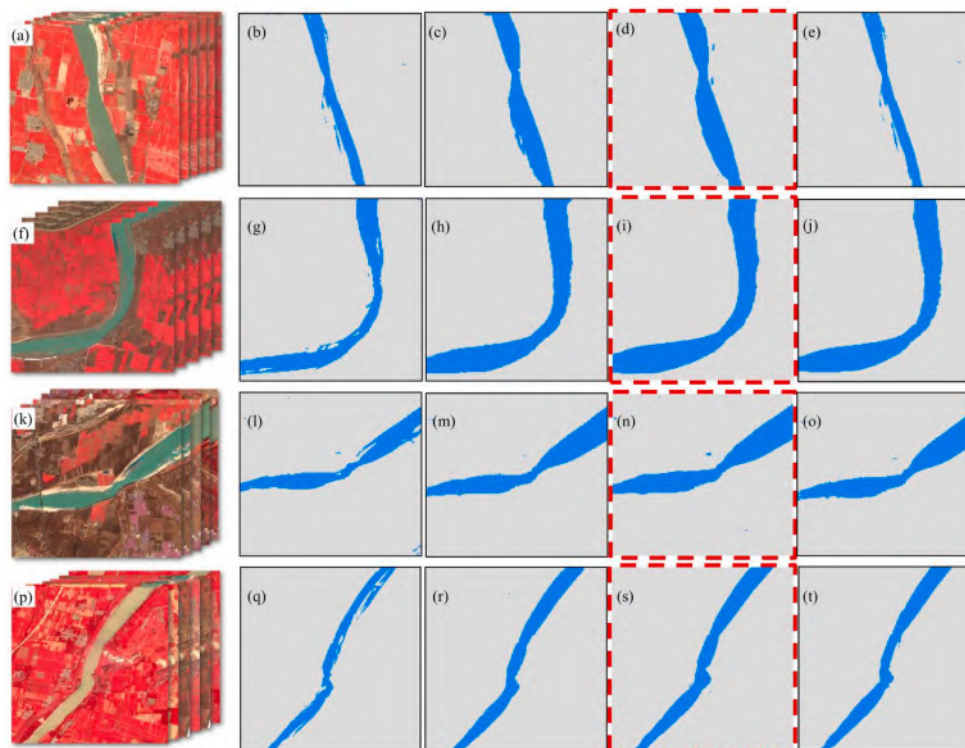

Step 1 Select the ROI with vegetation on both sides of the river (RW>90 m)

Step 2 Analyze the variation in backscatter intensity (σ) with the EVI and establish the functional relationships (**f1**)

Step 3 Calculate the backscatter coefficient after removing the factor of vegetation growth ($\sigma_{ROI,noveg}$) based on **f1 (Eq.3)**

$$\sigma_{ROI_{noveg}} = \frac{\sigma_W * A_W + mean(\sigma_{L,noveg}) * A_L}{A_{ROI}}$$

Establish the functional relationship between the water body percentage and $\sigma_{ROI,noveg}$ ($A_W/A_{ROI}\sim\sigma_{ROI,noveg}$)

Establish the functional relationship between FVC ratios and $\sigma_{ROI,noveg}$ ($FVC_{ROI}/FVC_{near}\sim\sigma_{ROI,noveg}$)

Step 4 Apply to mixed pixel scales and calculate river width based on A_W/A_{ROI}

$$W = \frac{A_W}{L} \quad (Eq.7)$$

Fig. 2. Flowchart of the RW-vebasud method.

Fig. 3. Selection of the region of interest (ROI) based on MNDWI. (a), (f), (k) and (p) represent long-term time series images of four different river sections synthesized from Sentinel-2 bands 8, 4, and 3; (b)-(e), (g)-(j), (l)-(o), and (q)-(t) represent the temporal variation of water surfaces extracted based on MNDWI for the four river sections, where the red dashed boxes indicate the maximum water extent. (For interpretation of the references to color in this figure legend, the reader is referred to the web version of this article.)

water body area. However, the vegetation area backscatter intensity is spatially and temporally unstable, making it difficult to calculate the backscatter intensity of water bodies. To overcome the impact of vegetation growth on σ in different seasons and locations, there is an urgent need to eliminate the impact of vegetation growth on the backscatter intensity and obtain the temporally and spatially stable vegetation area backscatter intensity to obtain the backscatter intensity of the water area.

The vegetation index (VI) is frequently employed as a means to indicate the status of vegetation growth, and widely used VIs include the normalized difference vegetation index (NDVI), EVI, soil adjusted vegetation index (SAVI), and perpendicular vegetation index (PVI) (Chen et al., 2021b; Gao et al., 2000). By utilizing the blue band, the EVI integrates a soil adjustment factor and an atmosphere resistance term. It solves the problems of easy saturation of the vegetation index and the lack of a linear relationship with actual vegetation cover. Thus, vegetation types can be distinguished well, and changes in vegetation structure and growth in different seasons and locations can be recognized (Gao et al., 2000). Volume scattering is the main mechanism accountable for backscatter from vegetation (Vreugdenhil et al., 2018). Research has demonstrated a strong correlation between EVI and variations in canopy structure, encompassing canopy type, plant physiognomy, and canopy architecture (Teixeira and Souza Filho, 2022; Wang et al., 2013). High correlations are often found between structural property indicators such as the EVI, biomass, LAI and cross-polarized backscatter at the C-band (Vreugdenhil et al., 2018). To eliminate the effect of vegetation growth on backscatter intensity, we established a correlation between σ and the EVI.

First, the MNDWI of the ROI was calculated based on Sentinel-2 data (Eq. 1) (Cordeiro et al., 2021; Xu, 2006), and the OTSU method was used to automatically extract the water threshold (Dong et al., 2021; Otsu, 1979), remove the water part in the ROI and obtain the nonwater part.

Then, the relationship between vegetation characteristics and σ was established in the nonwater part within the ROI range, that is, the relationship between the EVI and σ. Finally, considering this relationship, to eliminate the influence of vegetation growth factors on σ over time, the backscatter intensity σ_L of the nonwater part within each ROI after removing the influence of vegetation growth factors was determined.

(1) Extraction of the nonwater part

Compared to other indices, the MNDWI is generally less influenced by the subpixel vegetation component (Duan and Bastiaanssen, 2013). Hence, we opted to use the MNDWI for detecting water body changes here. Additionally, since the establishment of the EVI and σ relationship in this paper is based on large rivers (>90 m), the river width is much larger than the uncertainty from the MNDWI extracted water bodies, and ignoring the uncertainty of the MNDWI will not affect the accuracy of the subsequent results in this paper.

$$MNDWI = \frac{B3 - B11}{B3 + B11} \quad (1)$$

where B3 is the reflectance of the green band and B11 is the reflectance of the shortwave infrared band.

After the MNDWI was calculated, the water body threshold was automatically extracted using the OSTU method (Dong et al., 2021; Otsu, 1979) to identify the nonwater body fraction so that the relationship between the EVI and σ in this fraction could be explored further.

(2) Establishment of the relationship between EVI and σ

The vegetation backscatter intensity is unstable over time due to the changing vegetation structure and water content, which are the key

factors affecting backscatter intensity for the nonwater part (Land) of each ROI and are influenced by vegetation growth (Cui et al., 2022; Tao et al., 2016). To explore the correlation between vegetation growth and backscatter intensity and to eliminate the temporal instability, we selected 45 river sections with widths > 90 m and established the vegetation growth characterization index (EVI_L) and σ_L within the nonwater part or land for all time series (f1).

Both the NDVI and EVI can reflect vegetation growth changes, but soil background noise destroys the spatial consistency of the NDVI due to the more serious problem of red light saturation of NDVI data. In contrast, EVI addresses potential saturation effects in the red band under high biomass vegetation by incorporating the blue band, effectively reducing soil background noise. This makes EVI particularly suitable for monitoring dense or high biomass vegetation. Sentinel-2 data is used to calculate EVI (Eq. 2) (Gao et al., 2000) in this paper.

$$EVI = 2.5 \frac{\text{NIR} - \text{R}}{\text{NIR} + 6\text{R} - 7.5\text{B} + 1} \#(2)$$

where NIR, R, and B are the surface reflectance of NIR band (Band 8 for Sentinel-2), red band (Band 4) and blue band (Band 2), respectively. In addition, $EVI_{soil} \approx 0$. Backscatter intensity data were obtained from Sentinel-1 images.

(3) Elimination of the vegetation growth factor

As the backscatter intensity (σ) changes with vegetation growth in the above established EVI–σ functional relationship and terrestrial $EVI_L = 0$ represents the state of vegetation in the ROI when leaves are dry (which is considered as a state when vegetation is not growing), the backscatter intensity at this state can be regarded as that after removing the vegetation growth factor. $EVI_L = 0$ can represent the true cold, leaf-drop state in the deciduous vegetation zone and the assumed extreme leaf-drop state in the evergreen vegetation zone. Both indicate that there is no vegetation growth. Therefore, we extended the EVI (EVI_L) and backscatter intensity (σ_L) curves in the nonwater area in the reverse direction to obtain the corresponding σ_L value when EVI_L is 0, that is, the backscatter intensity of the nonwater part in the ROI of each site after removing the interference of vegetation growth ($\sigma_{L,noveg}$). Then, the total backscatter intensity ($\sigma_{ROI,noveg}$) (Eq. 3) in each ROI after removing the influence of vegetation growth no longer changes with vegetation but only with the water surface area (A_W) in the ROI. Thus, the effect of vegetation growth on the backscatter intensity is eliminated.

$$\sigma_{ROI,noveg} = \frac{\sigma_W * A_W + mean(\sigma_{L,noveg}) * A_L}{A_{ROI}} \#(3)$$

where $\sigma_{ROI,noveg}$ is the total backscatter intensity within each ROI after removing the effect of vegetation growth, A_{ROI} is the area of the ROI, A_W is the water body area within the ROI, i.e., (A_{ROI}-A_L), A_L is the area of nonwater body within the ROI, and σ_W is the backscatter intensity of water body. In this paper, we used the smallest backscatter intensity of randomly selected 100 water bodies points in the study area (0.000050) as σ_W. Natural features on the ground, like water, possess smooth surface and high dielectric constant, causing them to exhibit specular reflective characteristics. Consequently, the sensor receives a minimal amount of backscatter (DeVries et al., 2020).

In this paper, we screened ROI with cloudiness less than 20 % for 75 months from 01/2016–12/2021 for analysis following Eqs. 1–3, calculated the water body index according to Eq. 1, and extracted the nonwater body part within the ROI. Then, we calculated the EVI according to Eq. 2 and graded the nonwater body EVI data to obtain the total numbers of small, medium and large rivers in China based on the results of different time series EVI_L and σ_L for 197 river sections in China. An exponential function was fitted to EVI_L and σ_L because it best captured the relationship between these variables, leading to the functional relationship $\sigma_L = ae^{bEVI_L}$ for EVI_L and σ_L at each river section in the nine basins.

3.2.3. The establishment of the functional relationship of $A_W/A_{ROI} \sim \sigma_{ROI,noveg}$ (>90 m)

The overall backscatter intensity of a ROI is determined by the backscatter intensities of vegetation, soil, and water bodies, among which the backscatter intensity of water bodies is the lowest and relatively stable in time and space (DeVries et al., 2020). Thus, once the vegetation factor is removed, the larger the ratio of water bodies within the same ROI, the lower the overall backscatter intensity of the ROI. And the functional relationship between the water proportion and backscatter intensity was established on this basis. It is easier to detect changes in water surface area than in river width. Consequently, we first calculated the water surface area and then computed the river widths along a specific river reach following the approach outlined by Huang et al. (2018). The proportion of water in the ROI of all time series was calculated for each site, and the functional relationship of $A_W/A_{ROI} \sim \sigma_{ROI,noveg}$ (A_W is the area of water in the ROI) was fitted. Since σ_W is a constant value, Eq. 3 is further simplified as Eq. 4:

$$\sigma_{ROI,noveg} = \frac{mean(\sigma_W) * A_W + mean(\sigma_{L,noveg}) * A_L}{A_{ROI}}$$
$$= \frac{C * A_W + \sigma_{L,noveg} * (A_{ROI} - A_W)}{A_{ROI}} = (C - \sigma_{L,noveg}) * \frac{A_W}{A_{ROI}} + \sigma_{L,noveg} \#(4)$$

where A_W/A_{ROI} is the proportion of water bodies within the ROI and C is a constant, which is 0.000050 here. In addition, we assume there is no heterogeneity of backscatter intensity after removing the effect of vegetation growth in vegetation area i.e., mean ($\sigma_{L,noveg}$)= $\sigma_{L,noveg}$.

Since $\sigma_{L,noveg}$ per unit raster within the ROI of each river section is a constant value, it can be seen from Eq. 4 that $\sigma_{ROI,noveg}$ is a function of the proportion of water bodies within the ROI, and each section has a corresponding line due to the difference in $\sigma_{L,noveg}$. In other words, each section of the river has a corresponding linear relationship between the proportion of water bodies (A_W/A_{ROI}) and non-vegetated backscatter. Therefore, determining the $\sigma_{L,noveg}$ within an ROI will determine the proportion of water bodies (A_W/A_{ROI}) at this site and $\sigma_{ROI,noveg}$. When A_W/A_{ROI} is 100 %, $\sigma_{ROI,noveg}$ is equal to σ_W. When A_W/A_{ROI} is 0, $\sigma_{ROI,noveg}$ is equal to $\sigma_{L,noveg}$, and when the proportion of water bodies is 100 %, $\left(\frac{A_W}{A_{ROI}}, \sigma_{ROI}\right) = (1, \sigma_W) = (1, C)$, where C is constant, i.e., all the lines of river sections intersect as a point when the water body proportion is 100 %, as shown in Fig. 4.

3.2.4. The establishment of the functional relationship of $\sigma_{ROI,noveg} \sim FVC_{ROI}/FVCnear$ (>90 m)

After establishing the relationship between A_W/A_{ROI} and $\sigma_{ROI,noveg}$, we can calculate the proportion of water bodies at any site over time based on the ROI backscatter intensity ($\sigma_{ROI,noveg}$) that is not affected by vegetation growth by using the functional relationship. The backscatter intensity values of Sentinel-1 images include vegetation growth factors, and thus, $\sigma_{ROI,noveg}$ cannot be directly obtained (Bauer-Marschallinger et al., 2021). Thus, we calculated $\sigma_{ROI,noveg}$ by establishing a functional relationship between $FVC_{ROI}/FVCnear$ and $\sigma_{ROI,noveg}$. FVC reflects the proportion of surface vegetation greenness, and the surface vegetation type and growth rate are the main influencing factors. While the vegetation types of two adjacent areas are basically the same and the vegetation grows simultaneously, $FVC_{ROI}/FVCnear$ eliminates the influence of greenness and only reflects the proportion of surface water and land, and these factors influence the change in $\sigma_{ROI,noveg}$ after eliminating the vegetation growth (i.e., greenness influence). The overall backscatter intensity of the vegetation area is influenced by the water body proportion and vegetation growth factors (Zhou et al., 2019; DeVries et al., 2020). $FVC_{ROI}/FVCnear$ (where FVC_{ROI} is the ROI-inside-mixed and FVCnear is the ROI-neighboring-pixels mean FVC values) eliminates the influence of vegetation growth factors so that the overall backscatter
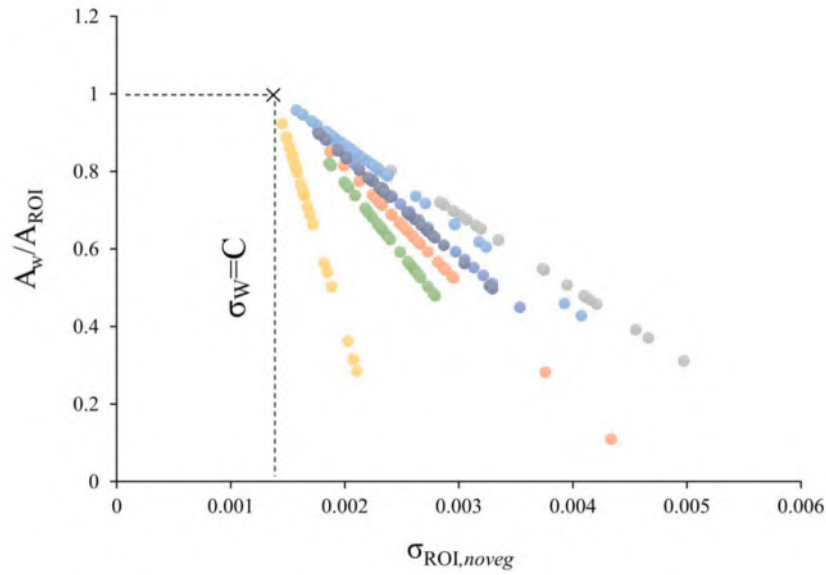
Figure 4. Relationship line of $A_W/A_{ROI} \sim \sigma_{ROI,noveg}$. C stands for constant. Points of different colors represent ROIs with different $\sigma_{L,noveg}$ values.

intensity of the ROI is only related to the change in water proportion (Fig. 5). Based on this, the functional relationship between the FVC ratio of two adjacent ROIs and $\sigma_{ROI,noveg}$ can be established, and then the values of $\sigma_{ROI,noveg}$ can be calculated.

Therefore, we established a relationship between the actual FVC_{ROI}/FVCnear and no vegetation growth disturbance $\sigma_{ROI,noveg}$ at all times within each ROI. Therefore, $\sigma_{ROI,noveg}$ for a given month can be obtained based on the FVC ratio for that month. The FVC_{ROI}/FVCnear $\sim \sigma_{ROI,noveg}$ line is only related to the variation in the water body ratio. The FVC is calculated as shown in Eq. 5 (Gutman and Ignatov, 1998; Yan et al., 2022).

$$FVC = \frac{(EVI - EVI_{min})}{(EVI_{max} - EVI_{min})} \#(5)$$

where the EVI is the enhanced vegetation index value, EVI_{max} represents the maximum EVI value in the area, while EVI_{min} denotes the minimum EVI value in the same area.

When choosing the neighboring pixels, to minimize the influence of human activities and to ensure that the vegetation types are basically the same as those in the ROI, the locations on both sides of the river where the ROI will not be flooded are chosen. This is shown in Fig. 5.

When the ROI is all water, the FVC of the ROI=0, i.e., FVC_{ROI}/FVCnear is 0, and the $\sigma_{ROI,noveg}$ at this point is σ_W. When the ROI is all land, the FVC_{ROI}/FVCnear is approximately equivalent to the ratio of the mean FVC of the nonwater body part of the ROI to the FVC of the neighboring pixels, and the $\sigma_{ROI,noveg}$ at this site is approximately equal to $\sigma_{L,noveg}$. Therefore, by determining $\sigma_{L,noveg}$ of a river section through a set of $EVI_L \sim \sigma_L$ functional relationships and then calculating the mean

Fig. 5. Selection of neighboring pixels (ROI width = maximum river width + 4 pixels).

FVC value of the nonwater part of the ROI and the neighboring pixel FVC ratio, the functional relationship of $FVC_{ROI}/FVCnear \sim \sigma_{ROI,noveg}$ in the river section can be determined. Each river section has an independent line (Fig. 6), and the starting FVC ratio of the line is 0.

3.2.5. River width calculation

When calculating the river width with RW-vebasud, the ROI and neighboring ROI are first determined. When the river width < satellite resolution (e.g., 10 m), the river section is located inside the mixed image element, a single pixel containing the river (mixed pixel) is selected as an ROI, and then one pixel to the left and right perpendicular to the river direction are selected as neighboring pixels. When the satellite resolution (10 m) < river width < 90 m, a single row of multiple pixels including the river width is selected as a single ROI, i.e., mixed pixel, and 1–2 pixels on the left and right sides are selected as neighboring pixels. When the river width > 90 m, 1–2 pixels close to the water body (extracted based on MNDWI) on both sides of the riverbank are selected as mixed images, and 1–2 images are extended outward perpendicular to the river direction as neighboring pixels. Then, the functional relationships of $A_W/A_{ROI} \sim \sigma_{ROI,noveg}$ (Fig. 4) and $FVC_{ROI}/FVCnear \sim \sigma_{ROI,noveg}$ (Fig. 6) are fitted, respectively. Finally, the above two functional relationships are combined to calculate the proportion of water bodies in any river section to obtain the river width. Details are as follows.

It is assumed that the vegetation types on both sides of the river in a mixed pixel are the same as those of its neighboring pixels. First, $\sigma_{L,noveg}$ of the nonwater part of the neighboring image is calculated based on the $EVI_L \sim \sigma_L$ functional relationship set (i.e., $\sigma_{L,noveg}$ of the mixed pixel). Next, Figs. 4 and Fig. 6 are used to determine the $A_W/A_{ROI} \sim \sigma_{ROI,noveg}$ lines corresponding to the mixed pixel and $FVC_{ROI}/FVCnear \sim \sigma_{ROI,noveg}$ line. Then, the ROI's FVC_{ROI} and the neighboring pixel's FVCnear of all time series are calculated. Since we assume that the mixed image element FVC is equal to the neighboring image element FVC when the mixed image element is all terrestrial, the $FVC_{ROI}/FVCnear$ range should be between 0 and 1. Therefore, we multiply the FVC_{ROI} by the corresponding adjustment factor α (Eq. 6) to ensure that the FVC_{ROI} is always smaller than the FVCnear. Finally, the $FVC_{ROI}/FVCnear$ of the mixed pixel for a certain month is calculated, and $\sigma_{ROI,noveg}$ of the river section is determined based on the $FVC_{ROI}/FVCnear \sim \sigma_{ROI,noveg}$ line (Fig. 6), followed by the proportion of the water body based on the $A_W/A_{ROI} \sim \sigma_{ROI,noveg}$ line of the river section (Fig. 4), which is the proportion

of the water body of the mixed pixel. The river width is calculated as shown in Eq. 7.

$$\alpha = \frac{FVC_{near} - 0.001}{FVC_{ROI}} \#(6)$$

where α is the adjustment factor, FVCnear is the neighboring pixel FVC value, 0.001 is the correction factor, and FVC_{ROI} is the mixed pixel FVC value.

$$W = \frac{A_W}{L} \#(7)$$

where W represents the mean width of the given river reach, A_W indicates the water surface area and L is the length of the river reach.

3.2.6. Application of the above RW-vebasud method to Sentinel

When using data from a Sentinel satellite to calculate the river width, which is less than the satellite resolution (10 m), the river is located inside mixed pixel, and the water body cannot be identified by satellite. Therefore, RW-vebasud can be applied directly to decompose the mixed pixel and obtain the water surface width.

For rivers where the width falls between 10 m and 90 m, only one or two pixels in the center of the river within the ROI can be identified. Decomposing mixed pixels with RW-vebasud can enhance the precision of water surface width extraction.

For rivers exceeding a width of 90 m, water surface width can be basically identified by satellite, but there are still mixed pixels on the left and right banks, which can be further decomposed by RW-vebasud to enhance the precision of estimating river width. The left and right banks are calculated independently, and the water surface widths of the two banks are determined separately. Finally, the total water surface widths are calculated based on Eq. 8:

$$w_f = w_s + w_l + w_r \#(8)$$

where w_f is the calculated water surface width at the river section, w_s is the water surface width extracted based on the MNDWI, w_l and w_r are the water surface width calculated by mixed pixel decomposition on the left and right bank.

3.2.7. Accuracy validation

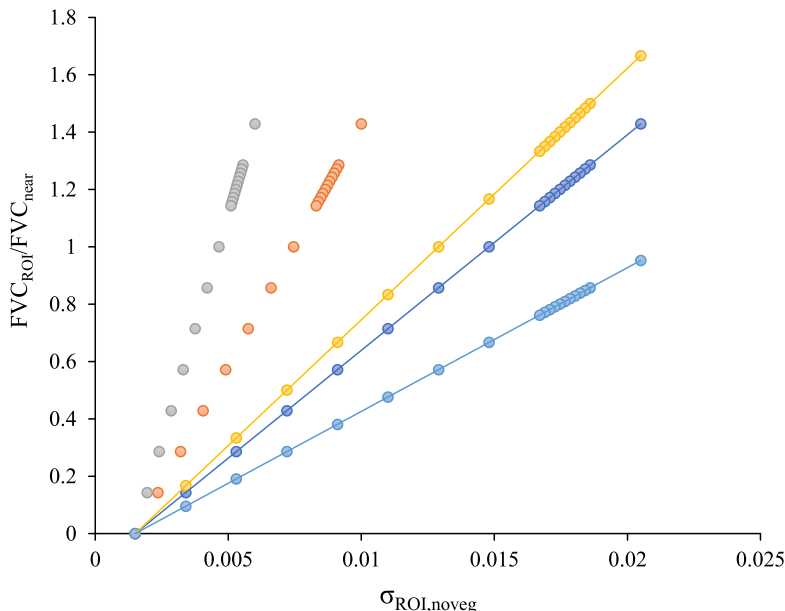The performance of RW-vebasud is ultimately assessed using the

Fig. 6. Relationship line between FVC_{ROI}/FVC_{near} and $\sigma_{ROI,noveg}$. Points of different colors represent ROIs with different $\sigma_{L,noveg}$ values.

Nash–Sutcliffe efficiency (NSE) index, root mean square error (RMSE), and percentage error (PE) following the research of Fabre et al. (2019) and Ling et al. (2019).

$$RMSE = \sqrt{\frac{1}{n}\sum_{i=1}^{n}|sim_i - obs_i|^2} \#(9)$$

$$NSE = 1 - \frac{\sum_{i-1}^{n}(obs_i - sim_i)^2}{\sum_{i-1}^{n}(obs_i - \overline{obs})^2} \#(10)$$

$$PE = \frac{1}{N}\sum_{i=1}^{N}\left(\frac{sim_i - obs_i}{obs_i}\right) \#(11)$$

where *obs* and *sim* represents measured and estimated data while $\overline{obs}$ is the observed data mean; and *n* is the number of sites.

4. Results

4.1. Mechanism analysis of the variation in σ with the EVI and the establishment of the correlation

The accuracy of the correlation between EVI_L and σ_L is influenced by the specific conditions of the study sites. Overall, EVI_L and σ_L showed a positive correlation, with an R^2 range of 0.16 to 0.69 and 75.61 % of the river sections above 0.40. The best fitting relationship between EVI_L and σ_L was found in the SLRB, with R^2 varies between 0.44 and 0.69, and some river sections in the southern basin had R^2 values below 0.40. On the one hand, this is related to the fact that the quality of Sentinel-2 visible light images is affected by cloudy weather and fog in southern China. Although images with less than 20 % clouds were selected in this paper, the percentage of clouds in the selected areas is still relatively high (>15 %), while it is only approximately 5 % in the north. On the

other hand, it is also due to the influence of different crops within the ROI, and the relationship between the two is more complicated than that of other vegetation due to the large variation in the EVI and σ in different growing periods of crops. In order to guarantee the precision of the simulation results, we only retained the curves with better fitting of σ with the EVI, i.e., the river sections with $R^2 > 0.40$ (i.e., R>0.6, P<0.005), to analyze the pervasive EVI–σ relationship.

In addition, based on the fitted functional relationship $\sigma_L = ae^{bEVI_L}$, we calculated σ_L ($\sigma_{L,noveg}$), i.e., the value of *a*, for each river section when the EVI_L is 0. The results show that $\sigma_{L,noveg}$ varies from basin to basin and is between 0.0014 and 0.15. The SLRB, INRB, HARB, and YLRB in northern China have low $\sigma_{L,noveg}$ values (0.0014–0.027). The HURB, YZRB, SWRB, SERB and PERB in South China have high $\sigma_{L,noveg}$ (0.0020 ~ 0.15). $\sigma_{L,noveg}$ reflects the condition of the underlying surface after removing the vegetation growth factor. The mean value of $\sigma_{L,noveg}$ differs greatly between the southern and northern watersheds in China, with the southern watershed (0.010) being 52 % higher than the northern (0.0048). The main reason for this is that the soil moisture (0–50 cm) in the south is 27.90 % higher than that in the north, with more precipitation in the south and generally higher soil water content (Zhang et al., 2016; Li et al., 2022).

After calculating σ_L, the backscatter intensity value $\sigma_{ROI,noveg}$ was calculated based on Eq. 3 for each ROI after removing the vegetation growth factor, which provides data that can be later analyzed to examine the functional relationship between proportion of water bodies and $\sigma_{ROI,noveg}$.

4.2. The establishment of the functional relationship of $A_W/A_{ROI} \sim \sigma_{ROI,noveg}$ (>90 m)

To analyze the relationship between the proportion of water bodies and the backscatter intensity after removing the vegetation growth
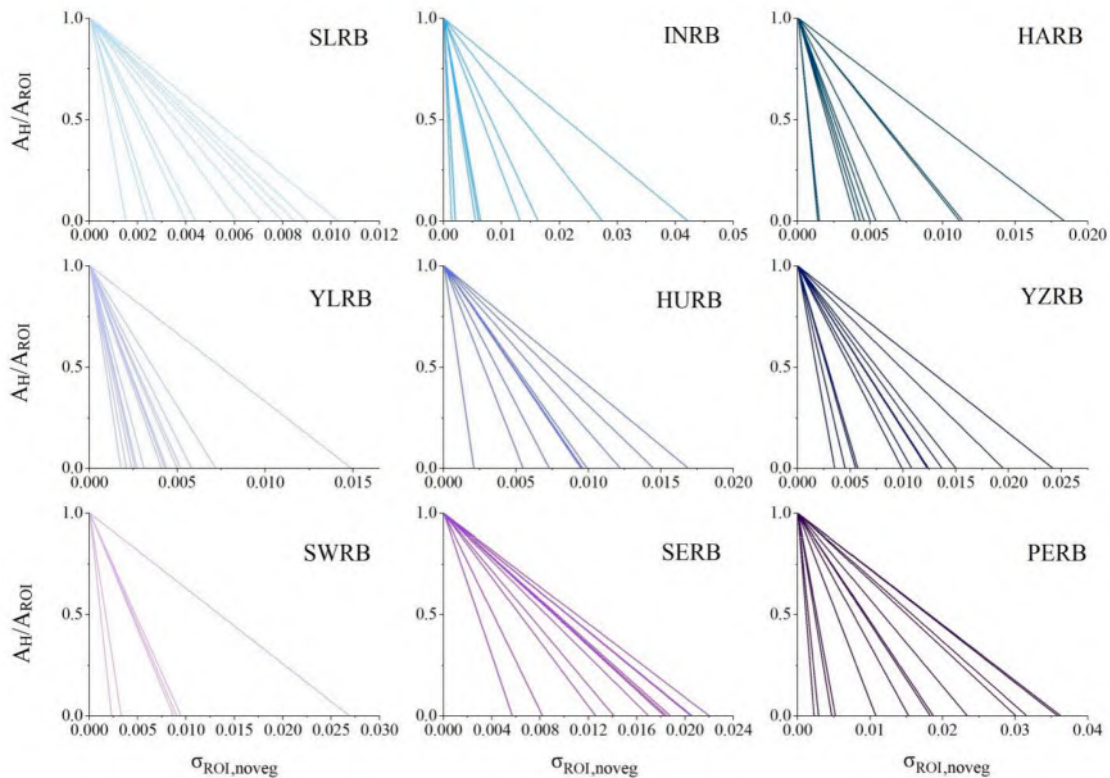
Fig. 7. Functional relation lines between A_W/A_{ROI} and $\sigma_{ROI,noveg}$ (SLRB: Songliao River Basin; INRB: Inland River basin; HARB: Hai River Basin; YLRB: Yellow River Basin; HURB: Huai River Basin; YZRB: Yangtze River Basin; SWRB: Southwest River Basin; SE: Southeast River Basin; and PERB: Pearl River Basin). (For interpretation of the references to color in this figure legend, the reader is referred to the web version of this article.)

factor, we established the A_W/A_{ROI}~$\sigma_{ROI,noveg}$ relationship line according to Fig. 7 based on the backscatter intensity value $\sigma_{ROI,noveg}$ calculated in Eq. 3. The results showed that A_W/A_{ROI} and $\sigma_{ROI,noveg}$ have a negative correlation, i.e., the value of $\sigma_{ROI,noveg}$ decreased as the water bodies area increased within the ROI. The slopes of the lines were different at different river sections within each basin (with different intercepts $\sigma_{ROI,noveg}$), i.e., the backscatter intensity $\sigma_{L,noveg}$ after removing vegetation disturbance was different at different river sections within the ROI (0.012 ± 0.0067) (Eq. 4). In addition, the range of variation of the $\sigma_{ROI,noveg}$ line was different in each basin, i.e., $\sigma_{L,noveg}$ was different. The range of variation of $\sigma_{L,noveg}$ in the SLRB was small (0.002 ~ 0.01), which is mainly due to the low heterogeneity of soil roughness and little variation of soil water content (0.15 ~ 0.35 m³/m³) in the SLRB (Li et al., 2022). In contrast, $\sigma_{ROI,noveg}$ had the largest range of variation within the INRB due to the large variation in soil water content within the basin (0–0.55 m³/m³) (Li et al., 2022). The river sections selected in this paper are spatially evenly distributed so that the river sections within each basin are representative of the overall characteristics of the basin. It can also be seen from Fig. 7 that the mean values of $\sigma_{ROI,noveg}$ were different in different basins. The PERB had the highest $\sigma_{ROI,noveg}$ value (0.020 ± 0.013), followed by the Southeast Basin (0.018 ± 0.0051). The YLRB had the lowest $\sigma_{ROI,noveg}$ values (0.0047 ± 0.0032).

After obtaining the A_W/A_{ROI}~$\sigma_{ROI,noveg}$ functional relationship (Fig. 7) for each river section, the $FVC_{ROI}/FVCnear$ ~ $\sigma_{ROI,noveg}$ functional relationship (Fig. 6) were further established to determine the $\sigma_{ROI,noveg}$ value. Then, the above two functional relationships were combined to calculate the proportion of water bodies at each river section.

4.3. The establishment of the functional relationship between $FVC_{ROI}/FVCnear$ and $\sigma_{ROI,noveg}$ (>90 m)

To calculate the proportion of water bodies after determining the $\sigma_{ROI,noveg}$ values at each river section through the A_W/A_{ROI}~$\sigma_{ROI,noveg}$ functional relationship, we established the $FVC_{ROI}/FVCnear$ ~ $\sigma_{ROI,noveg}$ functional relationship based on Fig. 6. First, $FVC_{ROI}/FVCnear$ (Eq. 5) was calculated for each river section of the nine basins for all time series, and the $FVC_{ROI}/FVCnear$ ~ $\sigma_{ROI,noveg}$ relationship line (Fig. 8) was fitted based on Fig. 6.

As shown in Fig. 8, a set of lines with different slopes was obtained for each basin. The $FVC_{ROI}/FVCnear$ values are positively correlated with $\sigma_{ROI,noveg}$, and $\sigma_{ROI,noveg}$ reached its maximum value when $FVC_{ROI}/FVCnear$ was at its maximum (i.e., no water bodies in the ROI). The $FVC_{ROI}/FVCnear$ values were different in different basins, and the $FVC_{ROI}/FVCnear$ values were lower in the SERB and HARB, i.e., the vegetation cover was similar in the mixed pixels and adjacent pixels, indicating that the vegetation distribution on both sides of the river was more uniform in these two basins.

The $FVC_{ROI}/FVCnear$ values of the SLRB, YZRB and SWRB were higher, i.e., the differences in vegetation cover in the mixed pixels and adjacent pixel were large, indicating that the vegetation cover on both sides of the river in the basin was different and unevenly distributed.
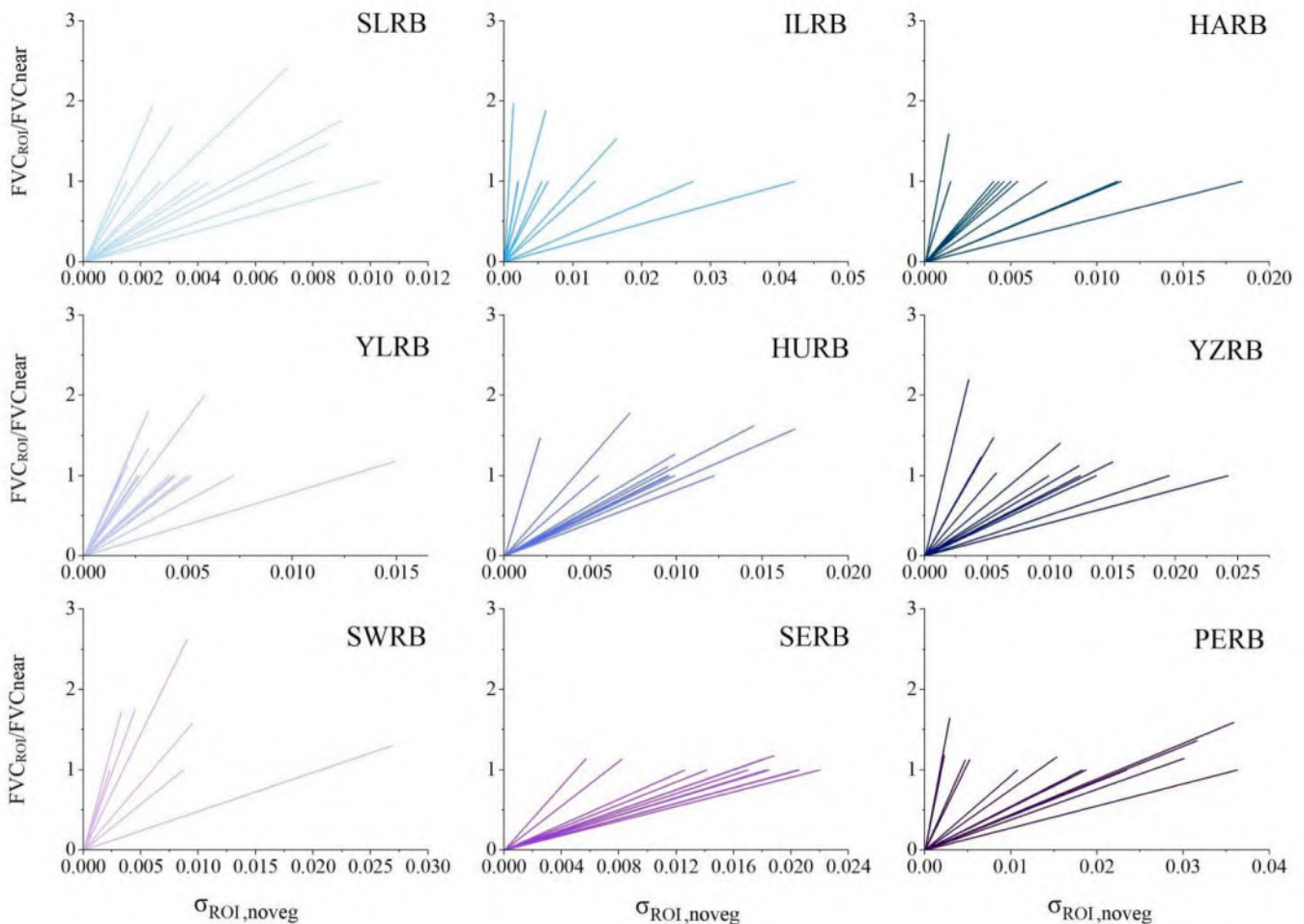

Fig. 8. Functional relation lines between $FVC_{ROI}/FVCnear$ and $\sigma_{ROI,noveg}$ (SLRB: Songliao River Basin; INRB: Inland River Basin; HARB: Hai River Basin; YLRB: Yellow River Basin; HURB: Huai River Basin; YZRB: Yangtze River Basin; SWRB: South–West River Basin; SE: South–East River Basin; and PERB: Pearl River Basin). (For interpretation of the references to color in this figure legend, the reader is referred to the web version of this article.)

After obtaining the FVC$_{ROI}$/FVCnear ~ $\sigma_{ROI,noveg}$ functional relationship, the FVC$_{ROI}$/FVCnear at the moment of image acquisition was calculated using Sentinel-2 images to determine the $\sigma_{ROI,noveg}$ at the corresponding time, and then the river width was calculated according to Eqs. 6–8.

4.4. Calculation results of river width in different phases for the last 6 years for each basin in China

Based on Eqs. 6–8, the river widths of 197 river sections were calculated, and the river width varied from 0.77 to 566.82 m. We calculated the river widths of nine river basins in China using the RW-vebasud method and explored the spatiotemporal distribution and variation patterns of the water surface width of Chinese rivers accordingly. Taking into account the climatic features, we concentrated on two seasons for all of China's rivers: the wet season (May to September) and the dry season (November to March). The spatiotemporal changes of river width in China between 2016 and 2021 were depicted based on the average width of major basins.

In general, the mean river width varied considerably among basins. Spatially, the rivers with larger six-year mean river widths mainly include the YZRB, PERB, YLRB, SLRB, and SWRB. The average river width in the YLRB was the largest (155.28 m), followed by the YZRB (91.63 m), and the HARB was the smallest (22.99 m). The uniformity of river width distribution also varied from basin to basin. The YZRB, HARB, HURB, etc., with a humid climate and relatively flat terrain had a relatively uniform distribution of river widths. The INRB rivers are un-evenly distributed due to topographic factors that determine the shape of river systems (dendritic, reticulated, radial, etc.). Rivers generally start in the high mountains and then flow downward along the terrain. The INRB is a mountainous and hilly area with undulating terrain, so the width of the river is unevenly distributed. Temporally, over the last 6 years, the average river width in China has shown an increase during both wet and dry seasons, with average increasing rates of 2.26 and 2.17 m/year, respectively. In wet season, the average river widths of the YZRB, HARB, HURB, YLRB and PERB displayed an increasing trend (P<0.05); in dry season, the average river widths of the YZRB, HARB, HURB, SWRB, YLRB and PERB showed an increasing trend (P<0.05) (Fig. 9). Affected by the Asian summer and winter monsoons, river widths also exhibit seasonal variations. For the YLRB, YZRB and SWRB, the mean absolute (relative) variation in river width was 32.34 m
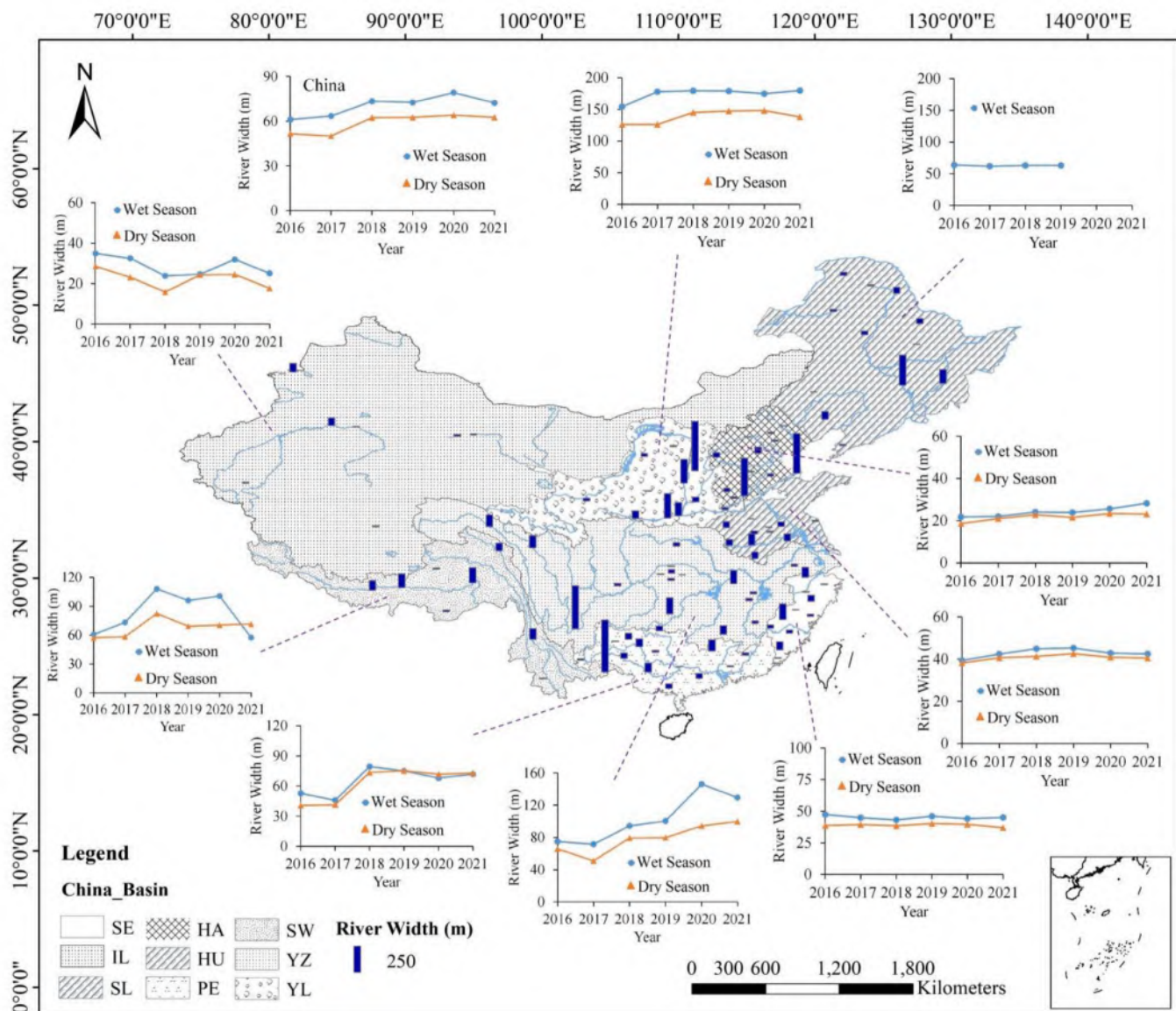

Fig. 9. Temporal and spatial distributions of river width in nine major river basins in China from 2016 to 2021.

(20.83 %), 23.71 m (25.87 %), and 14.73 m (19.66 %) in the dry and wet seasons, respectively. During the study period, most (72.03 %) of the rivers, such as the Yellow River, Hai River, and Huai River (Fig. 9), widened in summer.

4.5. Calculation and verification of river width at different scales (<10 m, 10 ~ 30 m, 30 ~ 90 m and > 90 m)

The river width results estimated by the proposed methods were compared with values measured in situ and estimated by the MNDWI. We segmented the statistics for different river widths (<10 m, 10 ~ 30 m, 30 ~ 90 m, >90 m) (Fig. 10c ~ j). The RMSEs extracted by the MNDWI method/calculated by RW-vebasud were 5.94/1.62 m, 9.84/3.19 m, and 12.95/5.42 m for river widths < 10 m, 10 ~ 30 m, and 30 ~ 90 m, respectively. When the river width is larger than 90 m, the RMSE difference was still large. The RMSE of RW-vebasud was 66.12 % lower than that of the MNDWI method. As shown in Fig. 10a, river widths less than 10 m (Sentinel-2 resolution) were not identified in the scatter plot of the water bodies obtained by Sentinel-2-based MNDWI extraction. By using RW-vebasud, the river width can be calculated at a subpixel scale of < 10 m. Overall, the improvement in NSE and the decrease in RMSE showed the effectiveness of RW-vebasud for river width measurement at the four scales with river widths of < 10 m, 10 ~ 30 m, 30 ~ 90 m and > 90 m.

Fig. 11 shows a comparison of the river width extracted directly by MNDWI and RW-vebasud methods when actually measured river width values are less than 90 m. The river widths of the water bodies extracted directly by the MNDWI of Sentinel-2/RW-vebasud were 0.80/0.96 for NSE, 9.03/3.83 m for RMSE, and 0.96/0.97 for R^2. The river widths obtained with RW-vebasud were more accurate than those extracted directly by the MNDWI. When the river widths of the water bodies were extracted directly by the MNDWI of Sentinel-2, the river widths were underestimated and deviated significantly (the mean relative error was

71 %), while the deviation was smaller (the mean relative error was 17 %) when using the RW-vebasud method (Fig. 11b).

To better compare the accuracy of river width estimation by MNDWI with those of RW-vebasud in this paper, we further analyzed the percentage error (PE) values for different river widths (Fig. 12). We found that the relative errors of river width estimation decreased with increasing river widths for both river width estimation methods. In general, the error in the estimated river width is primarily attributed to the presence of mixed pixels near the river boundary. Thus, the estimated error (the degree of estimated deviation) decreases as the river width increases. The results show that the relative errors of river widths estimated by MNDWI are always larger than those by RW-vebasud, as shown in Fig. 12. For rivers with widths wider than 90 m, the absolute PE values of river widths extracted by the MNDWI and estimated by our RW-vebasud method are all less than 25 %. While for rivers with widths less than 10 m, the PE values less than 25 % for river widths obtained by MNDWI estimation and based on RW-vebasud are 0 % and 58 %, respectively. It can be seen from Fig. 12 that the estimated result by MNDWI is always smaller than the actual river width by 71 % on average, which is associated with the limitation of satellite spatial resolution and the selection of the MNDWI water body threshold. It is a great challenge for the method to reasonably determine the threshold value.

5. Discussion

5.1. Analysis of the relationship between the EVI/proportion of water body/FVC ratio and σ

The results of this paper show that EVI_L and σ_L of the ROI time series show a positive correlation. This is corroborated by many scholars' studies; The research of Cui et al. (2022) in the Genhe watershed, China, demonstrated that the backscatter coefficient increases are caused by
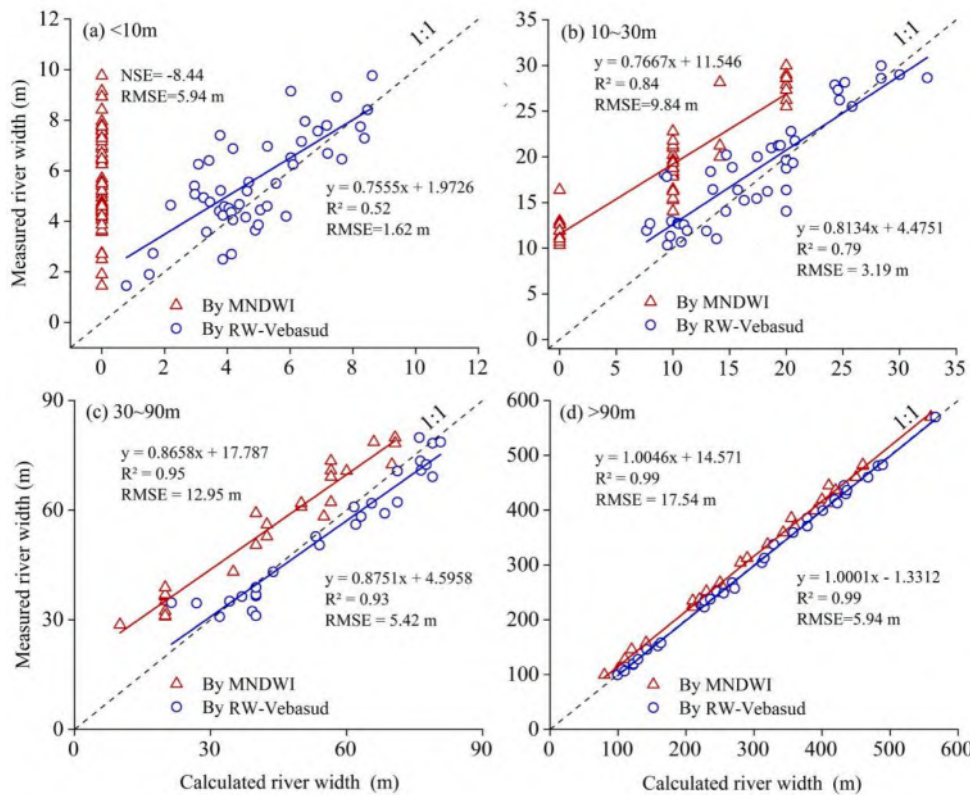

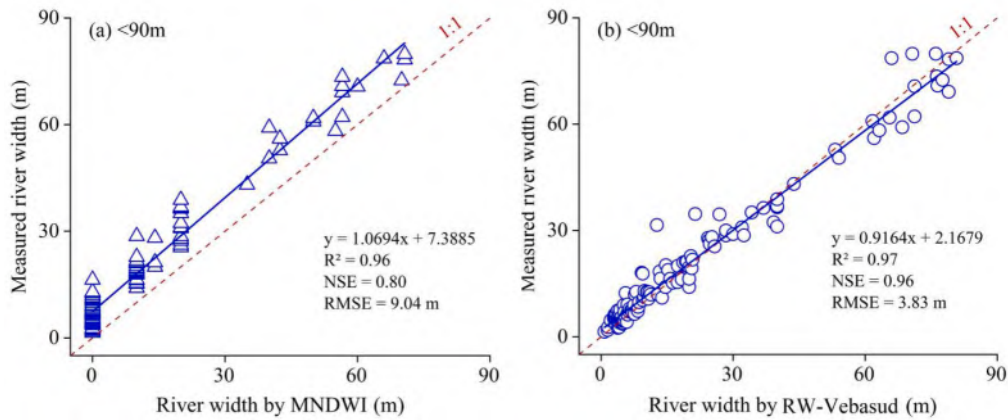**Fig. 10.** Estimation accuracy of the MNDWI method and RW-vebasud: (a) < 10 m; (b) 10 ~ 30 m; (c) 30 ~ 90 m; and (d) > 90 m.

Fig. 11. Estimation accuracy of the MNDWI method and RW-vebasud (<90 m): (a) MNDWI method and (b) RW-vebasud.
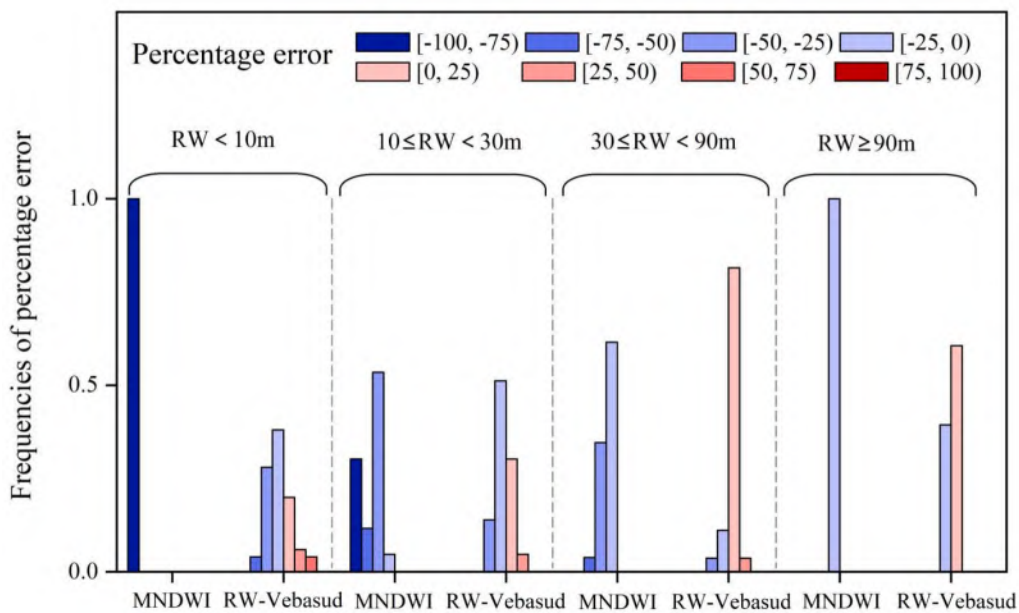

Fig. 12. Frequencies of different percentage errors for river width produced by satellite and the RW-vebasud method (RW is the river width, MNDWI means identified river width by the MNDWI, RW-vebasud means estimated river width using our method).

the direct scattering from the upper canopy, which is amplified as the scattering increase with the height of the canopy, and decreases due to the withering of vegetation. The research of Stendardi et al. (2019) in the South Tyrol Basin, Italy found that the cross-polarized VH backscatter coefficients obtained from Sentinel-1 satellite data exhibit a significant contribution from vegetation and demonstrate a strong correlation with the NDVI. The mechanism for positive correlation between EVI_L and σ_L is that the SAR backscatter signal intensity depends on dielectric (mainly controlled by moisture content) and geometric properties (e.g., surface roughness, vegetation canopy roughness, soil type and moisture, canopy water content, and canopy structure) of the target; So backscatter intensity within each ROI is influenced by the soil water content, vegetation water content, and vegetation canopy structure within that ROI, and the backscatter intensity changes with EVI as the vegetation growth changes (Canisius et al., 2018; DeVries et al., 2020). The positive correlation between EVI_L and σ_L in this paper means that from sparse to lush vegetation, with EVI increases volume scattering and canopy water content of vegetation increase, so does the backscatter intensity. Holtgrave et al. (2020) in Germany believes that the correlation between vegetation and SAR indices is also due to the fact that both

the two indices are influenced by biomass, which justified our results. However, Van Tricht et al. (2018) in Belgium holds different opinion that the increase in vegetation index correlates well with the decrease in predominantly VV backscatter as the plant undergoes its growth phase. The discrepancy attributes to the fact that their studies focused on crops while ours focused on natural vegetation. In other words, our method is more suitable for application in areas covered by natural vegetation. Selection of ROI should avoid croplands.

The R^2 of the fitted relationship between EVI_L and σ_L in this paper ranges from 0.44 to 0.69, and in some river sections of the southern watershed is below 0.40. The reason is that although the images with less than 20 % clouds were selected in this paper, the percentage of clouds in the selected satellite images of the southern region is still relatively high (>15 %), which is due to the rainy weather in the south and the difficulty to completely remove the clouds. This is consistent with researches from Domnich et al. (2021) in the Northern European terrestrial area which indicates that clouds pose the primary hindrances to regular land monitoring, greatly diminishing the practicality of optical satellite data. Li et al. (2021a) used satellite imagery to delineate river widths on the Yellow River and demonstrated that the presence of

cloud directly influences the quality of the satellite imagery, which further justified our results. On the other hand, the lack of a good fitting relationship between EVI_L and σ_L is also due to the multiple different crops within the ROI, as the relationship between the EVI and σ in different growing periods of crops is more complex compared to natural vegetation. For example, Nguyen et al. (2016) examined the correlation between the temporal changes in SAR backscatter and the growth cycle of rice plants in the Mekong Delta, Vietnam, and found that the back-scatter coefficients gradually increase during the growing period. Harfenmeister et al. (2019) explored SAR backscatter development in wheat and barley fields in Northeast Germany and found increasing signal attenuation due to the growth of vegetation during the spring season and stable signal attenuation once barley reached a specific height with the emergence of flag leaves. Specifically, the variety of crop species, the different crop structures, growing periods and water contents in different growing periods within ROIs lead to a low overall correlation between $EVI_L{\sim}\sigma_L$ (Nguyen et al., 2016; Whelen and Siqueira, 2017; Harfenmeister et al., 2019). In other words, $EVI_L{\sim}\sigma_L$ is not highly correlated in areas of intense human activity and is more applicable to natural vegetation areas with less human activity. Selection of ROI completely covered by natural vegetation will significantly improve the goodness of fitting relationship of $EVI_L{\sim}\sigma_L$.

In this paper, it is found that the water area proportion (A_W/A_{ROI}) is negatively correlated and FVC ratio ($FVC_{ROI}/FVCnear$) is positively correlated with the total backscatter intensity within each ROI after removing the effect of vegetation growth ($\sigma_{ROI,noveg}$). Our assumption is that the larger the proportion of water bodies in ROI is, the lower the backscatter intensity. Chen et al. (2021a) from China found that radar signals exhibit near-zero values over still water. Research of DeVries et al. (2020) utilized all accessible Sentinel-1 images to promptly depict surface inundation during flooding events in Greece, Houston and Texas, which found that the smooth, open water surfaces exhibit very low backscatter due to specular reflection. Soman and Indu (2022) use Sentinel-1 radar imagery to map inland water dynamics automatically in Madhya Pradesh, India and found that water has the lowest backscatter intensity. All these studies justified our assumption in this paper. However, White et al. (2015) reviewed several techniques to illustrate the potential of SAR for monitoring wetlands in Canada, found that waves in water often make water backscatter increased to values similar with land features. And Ramsey et al. (2013) utilized SAR data to monitor the occurrence of inundation in Louisiana coastal marshes and found that shallow water creates a rough water surface, thereby increasing the backscatter. In other words, floods and shallow water (depth < 20 cm) may introduce uncertainties into the river-width calculator and should be avoided when using our method.

5.2. Accuracy assessment

This paper found that the estimation accuracy of river width improved as the river width increased when using our method. Many scholars' studies are consistent with our findings, for instance, Ling et al. (2019) developed a method to measure river wet width (>5 m) at the subpixel scale based on Landsat imagery in the northwestern region of Oregon, USA, and found that the extent of overestimation and underestimation declined as the river width increased. Xue et al. (2022) proposed an automated method for extracting river width in the Loess Plateau, China, and found that the average error decreased as the river width increased. Compared with the MNDWI method, our RW-vebasud method demonstrates significant advantages when the river width is less than 90 m. This is because the MNDWI method cannot extract river widths smaller than 10 m based on current non-commercial satellite images. However, the RW-Vebasud method can as it is able to work at sub-pixel scales, enabling estimation of river widths less than 10 m. This demonstrates significant advantages of our method. Additionally, for river widths greater than 10 m, the MNDWI can extract but with poor accuracy (NSE=-1.78 and RMSE=9.84 for river widths of 10–30 m), and

only for river widths greater than 30 m the extraction will be more accurate. The reason for this is that the general river width extraction method is limited by the satellite resolution, which is usually more accurate when the river width exceeds three times the resolution of the satellite (Pavelsky and Smith, 2008; Yamazaki et al., 2014; Allen and Pavelsky, 2015; Feng et al., 2019; Li et al., 2021; Liang et al., 2022; Xue et al., 2022), but our RW-vebasud method can maintain high accuracy at less than 3x resolution (10–30 m) (NSE=0.70 and RMSE=3.19). This suggests that our study breaks through this internationally recognized 3 $\times$ resolution limitation and opens up new directions for fully exploiting satellite information. For remotely sensed imagery with a much higher spatial resolution, e.g., finer than 1 m, our method can further improve the monitored river width accuracy.

We also compared the RW-vebasud method with other sub-pixel decomposition methods derived from 10-meter resolution images. Bishop-Taylor et al. (2019) proposed a sub-pixel method for waterline extraction, achieving a good precision with a RMSE of 1.43 m when upscaling from 2-meter imagery to 10-meter ideal imagery for waterline extraction. Comparably, the RW-vebasud method has a RMSE of ${\sim}$ 0.81 m when used to extract water line. Zhou et al. (2023) used Bishop-Taylor's method to estimate river width along the Luo River (narrower than 500 m) in China, yielding a RMSE of 4.89 m. In contrast, the estimation using the RW-vebasud method resulted in a RMSE of 4.27 m. These highlight our method's advantage in the accuracy of river width calculation. In addition, Wang et al. (2022) introduced a method AHSWFM, yielding a RMSE of 0.04 m for natural and artificial water impoundments with average area ranging from 0.14 to 0.18 ha. We also applied our method to calculate water body areas for river segments of similar size range, yielding an estimated RMSE of 0.015, showing higher estimation accuracy. This again justified the accuracy of our method.

The findings demonstrate that the error in the river width estimation based on our RW-vebasud method is small and closer to the measured values. To further demonstrate this, we also compared the river width results > 30 m extracted by the RW-vebasud method with the currently publicly available river width datasets GRWL and MERIT Hydro (Fig. 13). From Fig. 13, we can find that the results obtained by RW-vebasud (NSE=0.99, RMSE=5.99 m, and $R^2 = 0.99$) outperform those with the GRWL datasets (NSE=0.93, RMSE=42.33 m, and $R^2 = 0.91$) and the MERIT Hydro datasets (NSE=0.87, RMSE=54.27 m, and $R^2 = 0.74$), which proves that our method is more accurate. This is because the GRWL dataset represents static river widths based on satellite imageries shot in mean-discharge months. Therefore, compared with real-time measured river width, our real-time estimation of river widths is more accurate. In addition, for rivers greater than 90 m, our estimate of river width (RMSE=5.94 m) is better than the NARWidth dataset by Allen and Pavelsky (2015), with an RMSE of 38 m. This is primarily because our use of Sentinel satellite imagery (10 m) provides higher resolution than Landsat satellite imagery (30 m) used in NARWidth dataset. This suggests the selection of satellite imageries with finer resolution can improve the accuracy of river width extraction. Moreover, our river width estimate is also better than the bankfull river width result of Li et al. (2021a) on the Yellow River, in which the RMSE of ours/Li's is estimated to be 5.86/7.455 m.

To analyze the reliability of our validation process, we compared it with the GRWL and MERIT Hydro river width datasets and found that the MERIT Hydro dataset underestimated. Yamazaki et al. (2014) conducted a study comparing river width with pre-existing datasets for the Mississippi and Congo Rivers, and the MERIT Hydro dataset's river width algorithm (global river width algorithm) was found to have a slightly underestimation, which is consistent with our validation process. Although our method demonstrates higher accuracy compared to the GRWL and MERIT datasets, it currently does not provide global river width measurements for non-vegetated areas like these two datasets, which is an area requiring further exploration
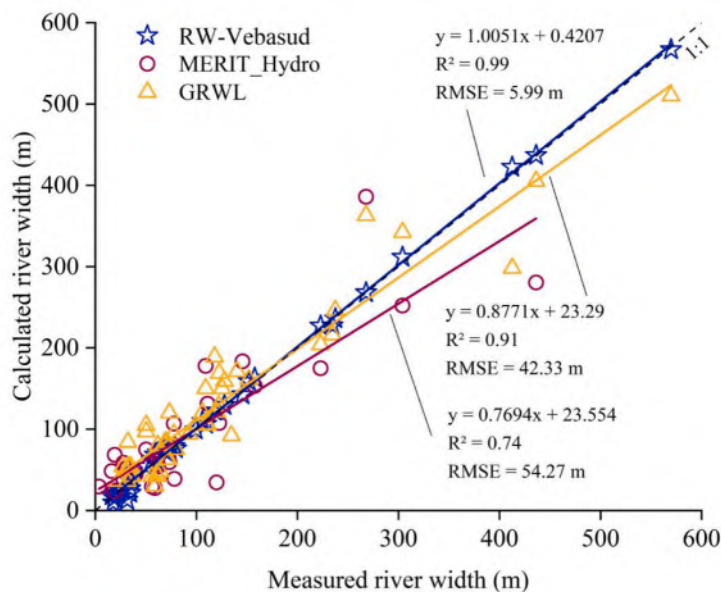
Fig. 13. Comparison of RW-vebasud calculated river widths with the GRWL and MERIT Hydro river width datasets.

5.3. Temporal and spatial variations in river width in China from 2016 to 2021

We found that the YLRB has the largest average river width, followed by the YZRB. In contrast, Yang et al. (2020) found that the average river widths in the SERB and YZRB were larger than in other basins when estimating river widths in nine major basins in China, which is inconsistent with our finding that the average river width in the YLRB was the largest. This is mainly because they mainly considered rivers larger than 30 m and did not include rivers smaller than 30 m in the YZRB and SERB, so the average river width of each basin was large. For further verification, we recounted the rivers with greater than 30 m river width in our results, and the average river width from largest to smallest is YZRB>SERB>YLRB, which is in accordance with the results reported by Yang et al. (2020). This proves the correctness of our results, and at the same time, our results include all types of rivers in the basin, i.e., large, medium and small rivers. In addition, the results are closer to reality, which shows that our study is more comprehensive in consideration and more reasonable in calculation.

The results of this paper show that the average river width increases in China from 2016 to 2021, while the river usually widens in summer during the year. In wet seasons, the increase in river width in the YZRB, HARB, YLRB, HURB, and PERB is attributed to the increased precipitation and flood intensity (Zhang et al., 2021; Su et al., 2016). For example, Zhang et al. (2021) examined the spatiotemporal variation in rainfall season precipitation characteristics in China from 1960 to 2018, revealing an increasing trend in heavy and very heavy precipitation during the rainy season. This justifies our results. In the dry season, the increased width of nonflood rivers in the YLRB and SWRB is associated with increased runoff due to accelerated glacial melting and increased annual precipitation on the Tibetan Plateau. Lutz et al. (2014) found that runoff is expected to increase for upstream SWRB until 2050 due to accelerated melting and heightened precipitation. Su et al. (2016) reported that the Mekong, Yellow, Salween, Yangtze, Brahmaputra, and Indus River Basins exhibit increasing trends in runoff, attributed to increased rainfall and glacier melting. These factors justify our study. The rivers widen in summer mainly as a result of the impact of the Asian monsoons (Wang et al., 2022). Moreover, it was found that the differences between wet and dry season river widths are larger in the YLRB, YZRB, and SWRB compared to other basins. This is due to a large contrast in precipitation levels between the dry and wet seasons in these

three basins, leading to a significant variance in runoff and, consequently, a marked distinction in river width (Wu et al., 2019; Wen et al., 2021). Especially in the global warming situation, the difference between dry and wet season precipitation is more obvious, and in most areas of China, the wet season is characterized by more concentrated precipitation, while the dry season experiences increased aridity (Yang et al., 2020).

Our study introduces $\sigma_{ROI,noveg}$ as an intermediate variable and indirectly calculates A_W/A_{ROI} from $FVC_{ROI}/FVCnear$ instead of directly calculates. The reason is that $\sigma_{ROI,noveg}$ is derived based on mechanistic processes and makes the whole A_W/A_{ROI} calculation process less empirical, avoiding the uncertainties introduced by satellite data noises when directly and empirically fitting A_W/A_{ROI} and $FVC_{ROI}/FVCnear$ using optical image data. On the other hand, the amount of available data obtained from optical images is small for areas heavily affected by cloud cover, making it difficult to establish the relationship between A_W/A_{ROI} and $FVC_{ROI}/FVCnear$. However, by introducing the intermediate variable $\sigma_{ROI,noveg}$ derived through mechanic formula derivation, the establishment of such relationships is easier and the accuracy is improved greatly.

Moreover, there is some uncertainty in the results of this paper, and further research is needed in the future. First, the accuracy of the results is still negatively influenced by clouds due to limitations in the cloud identification algorithm, although the current proportion of cloud images screened is less than 20 %. In the future, it is necessary to explore new ways for river width extraction based on SAR data from e.g. Sentinel-1, which is not disturbed by clouds. Second, the method proposed in this paper is currently only applicable to rivers with vegetation cover, excluding conditions of flood or shallow water (depth less than 20 cm). Exploration of the method for calculating river widths applicable to multiple types of substrates (e.g., both sides are rocky) is needed in the future. Finally, as the method requires the establishment of ROIs based on river locations for global application, accurate river positions are necessitated. Furthermore, it is worth noting that this study selected ROIs that are not affected by tree canopy shadows from overhead vegetation bordering the river, because the shadows on the water can change spectral reflectance and backscatter response. In future applications, it is necessary to eliminate tree shadows before use to ensure higher accuracy.

6. Conclusion

When the river width is larger than the satellite resolution, or hydraulically invisible, because of the presence of land–water mixed pixels, a small threshold of the MNDWI will lead to a large amount of land being extracted as water bodies, while a large threshold will easily lead to a small river width. Thus, it is a great challenge to determine the threshold reasonably. The present study proposed a subpixel decomposition method with a physical mechanism without relying on ground observations. Based on Sentinel-1 and -2 satellite images, we decomposed water–land mixed pixels to enhance the precision of river width inversion, applied the validated method to estimate the river widths of typical sections (including hydraulically invisible small rivers) in China's major basins from 2016 to 2021, and analyzed their spatial and temporal variation characteristics. The results show the following:

(1) Significantly breakthrough was made in reducing vegetation growth influence on the stability of the backscatter intensity and EVI relationship (σ-EVI). The EVI and backscatter intensity of vegetation zones within the ROI were positively correlated. Selection of ROI should avoid croplands. Completely covered by natural vegetation will significantly improve the goodness of fitting relationship of σ-EVI. (2) The river width calculated by RW-vebasud was more accurate than that directly extracted by the MNDWI, with the NSE increasing by more than 0.48 and the RMSE decreasing by $4.32 \sim 6.65$ m when the river width was less than 90 m. (3) The accuracy of RW-vebasud was better than that of the current well-known global river width datasets, GRWL and MERIT Hydro. For the RW-vebasud/GRWL/MERIT Hydro datasets, the NSE=0.99/0.93/0.87, RMSE=5.99/42.33/54.27, and $R^2 = 0.99/0.91/0.74$, respectively. (4) RW-vebasud maintained high accuracy (NSE=0.70 and RMSE=3.19) at less than three times the image resolution (10–30 m), breaking the internationally accepted limit that river width extraction is more accurate when the river width is less than three times the satellite resolution. In other words, our methods can be successfully applied to any spatial scale regardless of the spatial resolution of satellite imagery including both hydraulically invisible small and hydraulically visible large rivers. While floods may introduce uncertainties into the river-width calculator and should be avoided when using our method. (5) The Yellow River Basin (YLRB) (155.28 m on average) in China has the largest average river width, while the Hai River Basin (HARB, 22.99 m on average) has the smallest average river width including all types of rivers in the basin. (6) The average river width in the wet and dry seasons in China showed an increasing trend during $2016 \sim 2021$ and the rivers widen in summer mainly due to the impact of the Asian monsoons.

The outcome of this study can provide an effective method to extract river width at all scales by using satellite images, which can greatly reduce the uncertainties in river width calculations across the world. It also broke the bottleneck of strong spatial and temporal heterogeneity of σ-EVI, which resulted from vegetation growth making it impossible to establish a stable σ-EVI relationship and long-puzzled the global scientists. Moreover, it solved the problem of insufficient mechanisms in previous river width calculation methods, thereby avoiding the significant errors arose when applying them to small and medium-sized rivers. It might provide support for water resource assessments and water-related hazards. Noticeably, the method proposed in this paper is currently only works in vegetated areas. Additionally, this method can be attempted with other data sources. However, substituting with data of lower spatial resolution may decrease estimation accuracy.

CRediT authorship contribution statement

Maomao Li: Writing – original draft, Methodology, Data curation, Conceptualization. **Changsen Zhao:** Writing – review & editing, Supervision, Funding acquisition. **Zhen Duan:** Supervision, Resources. **Hongguang Cheng:** Supervision, Conceptualization. **Yanqing Lian:** Writing – review & editing, Project administration. **Guoqing Wang:** Supervision, Project administration.

Declaration of competing interest

The authors declare that they have no known competing financial interests or personal relationships that could have appeared to influence the work reported in this paper.

Data availability

Data will be made available on request.

References

Allen, G.H., Pavelsky, T.M., 2015. Patterns of river width and surface area revealed by the satellite-derived North American River Width data set. Geophys. Res. Lett. 42 (2), 395–402.

Allen, G.H., Pavelsky, T.M., 2018. Global extent of rivers and streams. Science 361 (6402), 585–587.

Allen, G.H., Pavelsky, T.M., Barefoot, E.A., Lamb, M.P., Butman, D., Tashie, A., Gleason, C.J., 2018. Similarity of stream width distributions across headwater systems. Nat. Commun. 9.

Bauer-Marschallinger, B., Cao, S., Navacchi, C., Freeman, V., Reuss, F., Geudtner, D., Rommen, B., Vega, F.C., Snoeij, P., Attema, E., Reimer, C., Wagner, W., 2021. The normalised Sentinel-1 Global Backscatter Model, mapping Earth's land surface with C-band microwaves. Sci. Data 8 (1), 277.

Canisius, F., Shang, J., Liu, J., Huang, X., Ma, B., Jiao, X., Geng, X., Kovacs, J.M., Walters, D., 2018. Tracking crop phenological development using multi-temporal polarimetric Radarsat-2 data. Remote Sens. Environ. 210, 508–518.

Chen, Y., Cao, R.Y., Chen, J., Liu, L.C., Matsushita, B., 2021b. A practical approach to reconstruct high-quality Landsat NDVI time-series data by gap filling and the Savitzky-Golay filter. ISPRS J. Photogramm. Remote Sens. 180, 174–190.

Chen, S.J., Huang, W.L., Chen, Y.M., Feng, M., 2021a. An adaptive thresholding approach toward rapid flood coverage extraction from sentinel-1 SAR imagery. Remote Sens. (basel) 13 (23).

Cordeiro, M.C.R., Martinez, J.-M., Peña-Luque, S., 2021. Automatic water detection from multidimensional hierarchical clustering for Sentinel-2 images and a comparison with Level 2A processors. Remote Sens. Environ. 253, 112209.

Cui, H.Z., Jiang, L.M., Paloscia, S., Santi, E., Pettinato, S., Wang, J., Fang, X.Y. and Liao, W.J. 2022. The Potential of ALOS-2 and Sentinel-1 Radar Data for Soil Moisture Retrieval With High Spatial Resolution Over Agroforestry Areas, China. Ieee Transactions on Geoscience and Remote Sensing 60.

DeVries, B., Huang, C., Armston, J., Huang, W., Jones, J.W., Lang, M.W., 2020. Rapid and robust monitoring of flood events using Sentinel-1 and Landsat data on the Google Earth Engine. Remote Sens. Environ. 240, 111664.

Domnich, M., Suenter, I., Trofimov, H., Wold, O., Harun, F., Kostiukhin, A., Jaerveoja, M., Veske, M., Tamm, T., Voormansik, K., Olesk, A., Boccia, V., Longepe, N., Cadau, E.G., 2021. KappaMask: AI-based cloudmask processor for sentinel-2. Remote Sens. (basel) 13 (20).

Dong, Z., Wang, G.J., Amankwah, S.O.Y., Wei, X.K., Hu, Y.F., Feng, A.Q., 2021. Monitoring the summer flooding in the Poyang Lake area of China in 2020 based on Sentinel-1 data and multiple convolutional neural networks. Int. J. Appl. Earth Obs. Geoinf. 102.

Duan, Z., Bastiaanssen, W.G.M., 2013. Estimating water volume variations in lakes and reservoirs from four operational satellite altimetry databases and satellite imagery data. Remote Sens. Environ. 134, 403–416.

Durand, M., Gleason, C.J., Pavelsky, T.M., Frasson, R.P.D., Turmon, M., David, C.H., Altenau, E.H., Tebaldi, N., Larnier, K., Monnier, J., Malaterre, P.O., Oubanas, H., Allen, G.H., Astifan, B., Brinkerhoff, C., Bates, P.D., Bjerklie, D., Coss, S., Dudley, R., Fenoglio, L., Garambois, P.A., Getirana, A., Lin, P.R., Margulis, S.A., Matte, P., Minear, J.T., Muhebwa, A., Pan, M., Peters, D., Riggs, R., Sikder, M.S., Simmons, T., Stuurman, C., Taneja, J., Tarpanelli, A., Schulze, K., Tourian, M.J., Wang, J.D., 2023. A framework for estimating global river discharge from the surface water and ocean topography satellite mission. Water Resour. Res. 59 (4).

Fabre, C., Sauvage, S., Tananaev, N., Noël, G., Teisserenc, R., Probst, J.L., Pérez, J., 2019. Assessment of sediment and organic carbon exports into the Arctic ocean: The case of the Yenisei River basin. Water Res. 158 (JUL.1), 118–135.

Feng, D.M., Gleason, C.J., Yang, X., Pavelsky, T.M., 2019. Comparing discharge estimates made via the BAM algorithm in high-order arctic rivers derived solely from optical cubesat, landsat, and sentinel-2 data. Water Resour. Res. 55 (9), 7753–7771.

Foody, G.M., Muslim, A.M., Atkinson, P.M., 2005. Super-resolution mapping of the waterline from remotely sensed data. Int. J. Remote Sens. 26 (24), 5381–5392.

Gao, X., Huete, A.R., Ni, W.G., Miura, T., 2000. Optical-biophysical relationships of vegetation spectra without background contamination. Remote Sens. Environ. 74 (3), 609–620.

Gorelick, N., Hancher, M., Dixon, M., Ilyushchenko, S., Thau, D., Moore, R., 2017. Google Earth Engine: Planetary-scale geospatial analysis for everyone. Remote Sens. Environ. 202, 18–27.

Gutman, G., Ignatov, A., 1998. The derivation of the green vegetation fraction from NOAA/AVHRR data for use in numerical weather prediction models. Int. J. Remote Sens. 19 (8), 1533–1543.

Harfenmeister, K., Spengler, D., Weltzien, C., 2019. Analyzing temporal and spatial characteristics of crop parameters using sentinel-1 backscatter data. Remote Sens. (basel) 11 (13).

Holtgrave, A.K., Roder, N., Ackermann, A., Erasmi, S., Kleinschmit, B., 2020. Comparing sentinel-1 and-2 data and indices for agricultural land use monitoring. Remote Sens. (basel) 12 (18).

Hou, J.W., van Dijk, A., Renzullo, L.J., Vertessy, R.A., Mueller, N., 2019. Hydromorphological attributes for all Australian river reaches derived from Landsat dynamic inundation remote sensing. Earth Syst. Sci. Data 11 (3), 1003–1015.

Huang, Q., Long, D., Du, M., Zeng, C., Qiao, G., Li, X., Hou, A., Hong, Y., 2018. Discharge estimation in high-mountain regions with improved methods using multisource remote sensing: a case study of the Upper Brahmaputra River. Remote Sens. Environ. 219, 115–134.

Li, Q.L., Shi, G.S., Shangguan, W., Nourani, V., Li, J.D., Li, L., Huang, F.N., Zhang, Y., Wang, C.Y., Wang, D.G., Qiu, J.X., Lu, X.J., Dai, Y.J., 2022. A 1 km daily soil moisture dataset over China using in situ measurement and machine learning. Earth Syst. Sci. Data 14 (12), 5267–5286.

Li, D., Wang, G., Qin, C., Wu, B.S., 2021. River extraction under bankfull discharge conditions based on sentinel-2 imagery and DEM data. Remote Sens. (basel) 13 (14).

Liang, X.A., Mao, W., Yang, K., Ji, L.Y., 2022. Automated Small River Mapping (ASRM) for the Qinghai-Tibet Plateau Based on Sentinel-2 Satellite Imagery and MERIT DEM. Remote Sens. (basel) 14 (19).

Lin, P.R., Pan, M., Allen, G.H., de Frasson, R.P., Zeng, Z.Z., Yamazaki, D., Wood, E.F., 2020. Global estimates of reach-level bankfull river width leveraging big data geospatial analysis. Geophys. Res. Lett. 47 (7).

Ling, F., Boyd, D., Ge, Y., Foody, G.M., Li, X.D., Wang, L.H., Zhang, Y.H., Shi, L.D., Shang, C., Li, X.Y., Du, Y., 2019. Measuring river wetted width from remotely sensed imagery at the subpixel scale with a deep convolutional neural network. Water Resour. Res. 55 (7), 5631–5649.

Liu, W., Zhang, X., He, F., Xiong, Q., Zan, X., Liu, Z., Sha, D., Yang, C., Li, S., Zhao, Y., 2021. Open-air grape classification and its application in parcel-level risk assessment of late frost in the eastern Helan Mountains. ISPRS J. Photogramm. Remote Sens. 174, 132–150.

Lu, Y.M., Wu, B.F., Yan, N.N., Zeng, H.W., Guo, Y., Zhu, W.W., Zhang, H., 2022. Method for monitoring environmental flows with high spatial and temporal resolution satellite data. Environ. Monit. Assess. 194 (1).

Lu, X., Yang, K., Bennett, M.M., Liu, C., Mao, W., Li, Y., Zhang, W.S., Li, M.C., 2021. High-resolution satellite-derived river network map reveals small Arctic river hydrography. Environ. Res. Lett. 16 (5).

Lutz, A.F., Immerzeel, W.W., Shrestha, A.B., Bierkens, M.F.P., 2014. Consistent increase in High Asia's runoff due to increasing glacier melt and precipitation. Nat. Clim. Chang.

Messager, M.L., Lehner, B., Cockburn, C., Lamouroux, N., Pella, H., Snelder, T., Tockner, K., Trautmann, T., Watt, C., Datry, T., 2021. Global prevalence of non-perennial rivers and streams. Nature 594 (7863), 391–397.

Nguyen, D.B., Gruber, A., Wagner, W., 2016. Mapping rice extent and cropping scheme in the Mekong Delta using Sentinel-1A data. Remote Sensing Letters 7 (12), 1209–1218.

Orusa, T., Cammareri, D., Borgogno Mondino, E., 2023. A possible land cover eagle approach to overcome remote sensing limitations in the alps based on sentinel-1 and sentinel-2: the case of Aosta Valley (NW Italy). Remote Sens. (basel) 15 (1), 178.

Otsu, N., 1979. Threshold selection method from gray-level histograms. IEEE Trans. Syst. Man Cybern. 9 (1), 62–66.

Pavelsky, T.M., Smith, L.C., 2008. RivWidth: A software tool for the calculation of river widths from remotely sensed imagery. IEEE Geosci. Remote Sens. Lett. 5 (1), 70–73.

Ramsey, E., Rangoonwala, A., Bannister, T., 2013. Coastal flood inundation monitoring with satellite C-band and L-band synthetic aperture radar data. J. Am. Water Resour. Assoc. 49 (6), 1239–1260.

Raymond, P.A., Hartmann, J., Lauerwald, R., Sobek, S., McDonald, C., Hoover, M., Butman, D., Striegl, R., Mayorga, E., Humborg, C., Kortelainen, P., Dürr, H., Meybeck, M., Ciais, P., Guth, P., 2013. Global carbon dioxide emissions from inland waters. Nature 503 (7476), 355–359.

Small, D., 2011. Flattening Gamma: Radiometric Terrain Correction for SAR Imagery. IEEE Trans. Geosci. Remote Sens. 49 (8), 3081–3093.

Soman, M.K., Indu, J., 2022. Sentinel-1 based Inland water dynamics Mapping System (SIMS). Environ. Model. Softw. 149, 105305.

Song, X.-P., Huang, W., Hansen, M.C., Potapov, P., 2021. An evaluation of Landsat, Sentinel-2, Sentinel-1 and MODIS data for crop type mapping. Sci. Remote Sens. 3, 100018.

Stendardi, L., Karlsen, S.R., Niedrist, G., Gerdol, R., Zebisch, M., Rossi, M., Notarnicola, C., 2019. Exploiting time series of sentinel-1 and sentinel-2 imagery to detect meadow phenology in mountain regions. Remote Sens. (basel) 11 (5).

Stumpf, A., Augereau, E., Delacourt, C., Bonnier, J., 2016. Photogrammetric discharge monitoring of small tropical mountain rivers: a case study at Riviere des Pluies, Reunion Island. Water Resour. Res. 52 (6), 4550–4570.

Su, F., Zhang, L., Ou, T., Chen, D., Yao, T., Tong, K., Qi, Y., 2016. Hydrological response to future climate changes for the major upstream river basins in the Tibetan Plateau. Global Planet. Change 136, 82–95.

Sun, W., Fan, J., Wang, G., Ishidaira, H., Bastola, S., Yu, J., Fu, Y.H., Kiem, A.S., Zuo, D., Xu, Z., 2018. Calibrating a hydrological model in a regional river of the Qinghai-Tibet plateau using river water width determined from high spatial resolution satellite images. Remote Sens. Environ. 214, 100–114.

Tao, L.L., Li, J., Jiang, J.B., Chen, X., 2016. Leaf Area Index Inversion of Winter Wheat Using Modified Water-Cloud Model. IEEE Geosci. Remote Sens. Lett. 13 (6), 816–820.

Tarpanelli, A., Mondini, A.C., Camici, S., 2022. Effectiveness of Sentinel-1 and Sentinel-2 for flood detection assessment in Europe. Nat. Hazards Earth Syst. Sci. 22 (8), 2473–2489.

Tarpanelli, A., Paris, A., Sichangi, A.W., O'Loughlin, F., Papa, F., 2023. Water resources in Africa: the role of earth observation data and hydrodynamic modeling to derive river discharge. Surv. Geophys. 44 (1), 97–122.

Teixeira, S.G., Souza Filho, P.W.Me., 2022. Seasonal variations in the backscatter of RADARSAT-1 images in tropical coastal environments. Braz. J. Geol. 52 (1), e20210077.

Van Tricht, K., Gobin, A., Gilliams, S., Piccard, I., 2018. Synergistic Use of Radar Sentinel-1 and Optical Sentinel-2 Imagery for Crop Mapping: A Case Study for Belgium. Remote Sens. (basel) 10 (10).

Verma, U., Chauhan, A., Pai, M.M.M., Pai, R., 2021. DeepRivWidth : Deep learning based semantic segmentation approach for river identification and width measurement in SAR images of Coastal Karnataka. Comput. Geosci. 154.

Vermote, E.F., Tanre, D., Deuze, J.L., Herman, M., Morcette, J.J., 1997. Second simulation of the satellite signal in the solar spectrum, 6S: an overview. IEEE Trans. Geosci. Remote Sens. 35 (3), 675–686.

Vollrath, A., Mullissa, A., Reiche, J., 2020. Angular-based radiometric slope correction for sentinel-1 on google earth engine. Remote Sens. (basel) 12 (11).

Vreugdenhil, M., Wagner, W., Bauer-Marschallinger, B., Pfeil, I., Teubner, I., Rudiger, C., Strauss, P., 2018. Sensitivity of sentinel-1 backscatter to vegetation dynamics: an Austrian case study. Remote Sens. (basel) 10 (9).

Wang, J., Ding, J., Li, G., Liang, J., Yu, D., Aishan, T., Zhang, F., Yang, J., Abulimiti, A., Liu, J., 2019. Dynamic detection of water surface area of Ebinur Lake using multi-source satellite data (Landsat and Sentinel-1A) and its responses to changing environment. Catena 177, 189–201.

Wang, X., Ge, L.L., Li, X.J., 2013. Pasture monitoring using SAR with COSMO-SkyMed, ENVISAT ASAR, and ALOS PALSAR in Otway. Australia. Remote Sensing 5 (7), 3611–3636.

Wang, B., Lin, Ho, 2002. Rainy season of the Asian-Pacific summer monsoon. J. Clim. 15 (4), 386–398.

Wang, Z.F., Liu, J.G., Li, J.B., Meng, Y., Pokhrel, Y., Zhang, H.S., 2021. Basin-scale high-resolution extraction of drainage networks using 10-m Sentinel-2 imagery. Remote Sens. Environ. 255.

Wang, J., Tang, Q., Chen, A., Tang, Y., Xu, X., Yun, X., Mu, M., Wright, N., Chen, D., 2022. Impacts of summer monsoons on flood characteristics in the lancang-mekong river basin. J. Hydrol. 604, 127256.

Wen, Z., Song, K., Shang, Y., Lyu, L., Tao, H., Liu, G., 2021. Natural and anthropogenic impacts on the DOC characteristics in the Yellow River continuum. Environ. Pollut. 287, 117231.

Whelen, T., Siqueira, P., 2017. Use of time-series L-band UAVSAR data for the classification of agricultural fields in the San Joaquin Valley. Remote Sens. Environ. 193, 216–224.

White, L., Brisco, B., Dabboor, M., Schmitt, A., Pratt, A., 2015. A Collection of SAR Methodologies for Monitoring Wetlands. Remote Sens. (basel) 7 (6), 7615–7645.

Wu, S.Q., Cao, S.S., Wang, Z.H., Qu, X.Y., Li, S.F., Zhao, W.J., 2019. Spatiotemporal Variations in Agricultural Flooding in Middle and Lower Reaches of Yangtze River from 1970 to 2018. Sustainability 11 (23).

Xu, H.Q., 2006. Modification of normalised difference water index (NDWI) to enhance open water features in remotely sensed imagery. Int. J. Remote Sens. 27 (14), 3025–3033.

Xue, Y., Qin, C., Wu, B.S., Li, D., Fu, X.D., 2022. Automatic Extraction of Mountain River Surface and Width Based on Multisource High-Resolution Satellite Images. Remote Sens. (basel) 14 (10).

Yamazaki, D., O'Loughlin, F., Trigg, M.A., Miller, Z.F., Pavelsky, T.M., Bates, P.D., 2014. Development of the global width database for large rivers. Water Resour. Res. 50 (4), 3467–3480.

Yamazaki, D., Ikeshima, D., Sosa, J., Bates, P.D., Allen, G.H., Pavelsky, T.M., 2019. MERIT Hydro: a high-resolution global hydrography map based on latest topography dataset. Water Resour. Res. 55 (6), 5053–5073.

Yan, K., Gao, S., Chi, H.J., Qi, J.B., Song, W.J., Tong, Y.Y., Mu, X.H., Yan, G.J., 2022. Evaluation of the vegetation-index-based dimidiate pixel model for fractional vegetation cover estimation. IEEE Trans. Geosci. Remote Sens. 60.

Yang, J., Huang, X., Tang, Q.H., 2020. Satellite-derived river width and its spatiotemporal patterns in China during 1990–2015. Remote Sens. Environ. 247.

Yesou, H., Pottier, E., Mercier, G., Grizonnet, M., Haouet, S., Giros, A., Faivre, R., Huber, C., Michel, J. and Ieee 2016 Synergy of Sentinel-1 and Sentinel-2 Imagery for Wetland Monitoring Information Extraction from Continuous Flow of Sentinel Images Applied to Water Bodies and Vegetation Mapping and Monitoring, pp. 162-165, Beijing, PEOPLES R CHINA.

Yin, Z.X., Ling, F., Li, X.Y., Cai, X.B., Chi, H., Li, X.D., Wang, L.H., Zhang, Y.H., Du, Y., 2022. A cascaded spectral-spatial CNN model for super-resolution river mapping With MODIS imagery. IEEE Trans. Geosci. Remote Sens. 60.

Yu, Z., An, Q., Liu, W., Wang, Y., 2022. Analysis and evaluation of surface water changes in the lower reaches of the Yangtze River using Sentinel-1 imagery. J. Hydrol.: Reg. Stud. 41, 101074.

Zhang, L., Lu, H., Wang, L., Yang, B., 2016. Spatial-temporal characteristics of soil moisture in China. Acta Geograph. Sin. 71 (9), 1494–1508.

Zhang, Y.Y., Zang, S.Y., Shen, X.J., Fan, G.H., 2021. Observed Changes of Rain-Season Precipitation in China from 1960 to 2018. Int. J. Environ. Res. Public Health 18 (19).

Zhao, C., Pan, T., Dou, T., Liu, J., Liu, C., Ge, Y., Zhang, Y., Yu, X., Mitrovic, S., Lim, R., 2019. Making global river ecosystem health assessments objective, quantitative and comparable. Sci. Total Environ. 667, 500–510.

Zhou, Z.W., Liu, L., Jiang, L.M., Feng, W.P., Samsonov, S.V., 2019. Using Long-Term SAR Backscatter Data to Monitor Post-Fire Vegetation Recovery in Tundra Environment. Remote Sens. (basel) 11 (19).